

THE TEXES SURVEY FOR H₂ EMISSION FROM PROTOPLANETARY DISKS

MARTIN A. BITNER^{1,2}, MATTHEW J. RICHTER^{2,3}, JOHN H. LACY^{1,2}, GREGORY J. HERCZEG⁴, THOMAS K. GREATHOUSE^{2,5}, DANIEL T. JAFFE^{1,2}, COLETTE SALYK⁶, GEOFFREY A. BLAKE⁶, DAVID J. HOLLENBACH⁷, GREG W. DOPPMANN⁸, JOAN R. NAJITA⁸, THAYNE CURRIE⁹

Draft version September 6, 2021

ABSTRACT

We report the results of a search for pure rotational molecular hydrogen emission from the circumstellar environments of young stellar objects with disks using the Texas Echelon Cross Echelle Spectrograph (TEXES) on the NASA Infrared Telescope Facility and the Gemini North Observatory. We searched for mid-infrared H₂ emission in the S(1), S(2), and S(4) transitions. Keck/NIRSPEC observations of the H₂ S(9) transition were included for some sources as an additional constraint on the gas temperature. We detected H₂ emission from 6 of 29 sources observed: AB Aur, DoAr 21, Elias 29, GSS 30 IRS 1, GV Tau N, and HL Tau. Four of the six targets with detected emission are class I sources that show evidence for surrounding material in an envelope in addition to a circumstellar disk. In these cases, we show that accretion shock heating is a plausible excitation mechanism. The detected emission lines are narrow (~ 10 km s⁻¹), centered at the stellar velocity, and spatially unresolved at scales of 0.4'', which is consistent with origin from a disk at radii 10-50 AU from the star. In cases where we detect multiple emission lines, we derive temperatures $\gtrsim 500$ K from $\sim 1 M_{\oplus}$ of gas. Our upper limits for the non-detections place upper limits on the amount of H₂ gas with T > 500 K of less than a few Earth masses. Such warm gas temperatures are significantly higher than the equilibrium dust temperatures at these radii, suggesting that the gas is decoupled from the dust in the regions we are studying and that processes such as UV, X-ray, and accretion heating may be important.

Subject headings: circumstellar matter, infrared:stars, stars:planetary systems, protoplanetary disks, stars:individual(AB Aur, DoAr 21, Elias 29, GSS 30 IRS 1, GV Tau N, HL Tau), stars:pre-main sequence

1. INTRODUCTION

Studying the structure and evolution of circumstellar disks is crucial to developing an understanding of the process of planet formation. Observations of dust emission and modeling of the spectral energy distributions (SED) of disks have revealed much about the dust component from a few stellar radii out to hundreds of AU (Zuckerman 2001). While circumstellar disks are composed of both dust and gas, the gas component dominates the mass of the disk, with molecular hydrogen (H₂) being the most abundant constituent. In order to develop a complete picture of the structure and evolution of protoplanetary disks, it is important to observe the gas.

Observations at different wavelengths probe different disk radii. Submillimeter observations sample gas at large radii (> 50 AU) (Semenov et al. 2005), while near-

infrared CO (Najita et al. 2003; Blake & Boogert 2004) and H₂O (Carr et al. 2004; Thi & Bik 2005) observations allow for study of the inner few AU. Spectral lines in the mid-infrared (5-25 μ m) provide a means to investigate gas in the giant planet region of the disk and beyond (10-50 AU) (Najita et al. 2007a).

Several mid-infrared spectral diagnostics have been shown to be useful probes of gas in disks. These include [NeII] at 12.8 μ m (Pascucci et al. 2007; Lahuis et al. 2007; Herczeg et al. 2007), H₂O rotational transitions (Carr & Najita 2008; Salyk et al. 2008), [FeI] at 24 μ m (Lahuis et al. 2007), and, based on a theoretical analysis of debris disks, [Si] at 25.2 μ m, and [FeII] at 26 μ m (Gorti & Hollenbach 2004).

Molecular hydrogen should make up the bulk of the mass in disks, but is a challenge to detect. Bright far-ultraviolet (FUV) H₂ emission from classical T Tauri stars may be produced in the irradiated disk surface (Herczeg et al. 2002; Bergin et al. 2004). At longer wavelengths, rovibrational and pure rotational transitions are generally weak because H₂ lacks a permanent dipole moment. Near-infrared emission in the $v=1-0$ S(1) rovibrational transition of H₂ has been detected from T Tauri stars (Bary et al. 2003; Ramsay Howat & Greaves 2007; Carmona et al. 2008b) and may be the result of excitation by UV and X-ray irradiation (Nomura et al. 2007; Gorti & Hollenbach 2008). Near-infrared adaptive optics fed, integral field spectroscopy of six classical T Tauri stars that drive powerful outflows has revealed that most of the H₂ emission is spatially extended from the con-

¹ Space Telescope Science Institute, Baltimore, MD; mbitner@stsci.edu

² Visiting Astronomer at the Infrared Telescope Facility, which is operated by the University of Hawaii under Cooperative Agreement no. NCC 5-538 with the National Aeronautics and Space Administration, Science Mission Directorate, Planetary Astronomy Program.

³ Physics Department, University of California at Davis, Davis, CA

⁴ California Institute of Technology, Pasadena, CA

⁵ Southwest Research Institute, San Antonio, TX

⁶ Division of Geological & Planetary Sciences, California Institute of Technology, MS 150-21, Pasadena, CA

⁷ NASA Ames Research Center, Moffett Field, CA

⁸ National Optical Astronomy Observatory, Tucson, AZ

⁹ Harvard-Smithsonian Center for Astrophysics, Cambridge, MA

tinuum (Beck et al. 2008). The properties of the emission are consistent with shock excitation from outflows or winds rather than UV or X-ray excitation from the central star. The FUV H_2 emission probes gas between 2000 and 3000 K (Herczeg et al. 2004; Nomura & Millar 2005) and the $2.12 \mu\text{m}$ H_2 line traces gas at $T > 1000$ K (Bary et al. 2003). The mid-infrared H_2 lines considered in this paper are most sensitive to gas at lower temperatures.

Owing to their small Einstein A-values, the pure rotational mid-infrared H_2 lines remain optically thin to large column densities ($N_{H_2} > 10^{23} \text{ cm}^{-2}$) and will be in LTE at the densities found in disks. For a disk with a strong mid-infrared continuum, the dust becomes optically thick well before the H_2 lines. Observable line emission is present only when there is a temperature inversion in the atmosphere of the disk or if there is a layer of dust-depleted gas separate from the optically thick dust. The process of dust coagulating into larger grains or settling out of the disk atmosphere can allow a larger column of gas to be observed. A disk that has an optically thin mid-infrared continuum, implying a very small amount of dust in the disk or dust grains that have grown large compared to mid-infrared wavelengths, would allow the entire disk to be observable. However, it is not known whether such disks have large quantities of gas and, in the absence of gas heating through collisions with dust grains, another heating mechanism is necessary in dust-free environments, such as UV or X-ray heating (Glassgold et al. 2004; Gorti & Hollenbach 2004; Nomura et al. 2007).

A number of groups have searched for H_2 emission from protoplanetary disks in recent years. Thi et al. (2001) reported the detection of several Jupiter masses of warm gas in a sample of disk sources based on *Infrared Space Observatory* (ISO) observations of the H_2 S(0) and S(1) lines. However, follow-up observations from the ground with improved spatial resolution did not confirm these results (Richter et al. 2002; Sheret et al. 2003; Sako et al. 2005). Richter et al. (2002) used the Texas Echelon Cross Echelle Spectrograph (TEXES) on the NASA 3m Infrared Telescope Facility (IRTF) to set upper limits on the warm gas mass within the disks of six young stars. Sheret et al. (2003) searched for H_2 emission using MICHELLE on the United Kingdom Infrared Telescope and set upper limits on the emission from disks around two stars. The first group to use an 8-meter class telescope in the search for molecular hydrogen was Sako et al. (2005) using the Cooled Mid-Infrared Camera and Spectrometer on the 8.2 m Subaru telescope to set upper limits for emission in the S(1) line around four young stars. Using the Infrared Spectrograph (IRS) aboard the *Spitzer Space Telescope*, Pascucci et al. (2006) reported the non-detection of H_2 lines in their sample of 15 young Sun-like stars, while Lahuis et al. (2007) detected the S(2) and S(3) lines in $\sim 8\%$ of the 76 circumstellar disks in their sample. Recently, ground-based observations with high resolution spectrometers on 8-meter class telescopes have produced both detections of the mid-infrared H_2 lines in the Herbig Ae stars AB Aur and HD 97048 (Bitner et al. 2007; Martin-Zaidi et al. 2007) and stringent upper limits in a sample of six Herbig Ae/Be stars and one T Tauri star (Carmona et al. 2008a).

Three mid-infrared pure rotational H_2 lines are observable from the ground: S(1) ($\lambda = 17.035 \mu\text{m}$), S(2) ($\lambda = 12.279 \mu\text{m}$), and S(4) ($\lambda = 8.025 \mu\text{m}$). When multiple optically thin lines are observed, line ratios permit the determination of the temperature and mass of the emitting gas. Ratios of these three lines are most sensitive to temperatures of 200-800 K. Two additional pure rotational H_2 lines are observable near $5 \mu\text{m}$: S(8) ($\lambda = 5.053 \mu\text{m}$) and S(9) ($\lambda = 4.695 \mu\text{m}$), extending our temperature sensitivity to hotter gas. The high spectral resolution possible with an instrument like TEXES (Lacy et al. 2002) increases our sensitivity to narrow line emission and helps determine the location of the emission. By making observations at high spectral resolution, we maximize the line to continuum contrast while minimizing atmospheric effects by separating the lines from nearby telluric features. A further benefit of high spectral resolution is that we are able to estimate the location of the emitting gas if coming from a disk under the assumption of Keplerian rotation.

In this paper, we present the results of a search for molecular hydrogen emission in disk sources using TEXES on both the IRTF and Gemini North telescopes. We observed 29 sources spanning a range of mass, age, and accretion rate in order to constrain the amount of warm gas in the circumstellar disks of these stars.

2. OBSERVATIONS AND DATA REDUCTION

We observed 29 sources using TEXES on both the NASA IRTF telescope during 2002-2005 and on Gemini North in 2006 and 2007 under program IDs GN-2006A-DS-3, GN-2006B-Q-42, and GN-2007B-C-9. The spectral resolution of the observations was $\gtrsim 60,000$ for the S(1) line and $\gtrsim 80,000$ for the S(2) and S(4) lines. Due to telluric absorption from water vapor close to the S(1) and S(2) lines, we observed these settings both when telluric water vapor levels were low and the Earth's motion gave an additional redshift towards the source. Removal of background sky emission was achieved by nodding the source along the slit and subtracting nod pairs. On the IRTF, the TEXES slit widths were $2''$ at the S(1) setting and $1.4''$ at S(2) and S(4). For our Gemini observations, the slit widths were $0.81''$ at S(1) and $0.54''$ at S(2) and S(4).

We observed telluric standards at each setting for use as divisors to correct the spectra for atmospheric absorption. Asteroids work well as telluric calibrators at 12 and $17 \mu\text{m}$, while we used early-type stars at $8 \mu\text{m}$. We observed flux standards for some sources. Where possible, however, we normalized the continuum level to agree with photometric measurements obtained from *Spitzer*, *ISO*, or ground-based observations. Tables 2, 4, and 5 list references for the continuum fluxes. Data reduction was carried out using the standard TEXES pipeline (Lacy et al. 2002).

Our sample was chosen to include sources with a range in age, accretion rate, and mass. Included among our targets are class I sources with both a remnant envelope and a disk, classical T Tauri stars with optically thick disks, T Tauri stars with optically thin disks or inner holes, stars with high accretion rates such as FU Ori and Z CMa, Herbig Ae stars with more massive disks, as well as the debris disk around the star 49 Ceti. The combination of TEXES with Gemini has allowed us to extend our

survey to sources with mid-infrared continuum levels of a few tenths of a Jansky. Since the mid-infrared continuum comes from warm dust grains, this allows the inclusion of sources without much dust where larger columns of gas may be observable as long as there are additional heating mechanisms beyond gas/dust heating. Properties of the targets in our sample are listed in Table 1.

Observations of the H₂ S(9) line for a subset of our sample were carried out between 2000 and 2005 using NIRSPEC on the Keck telescope as part of an ongoing M-band survey (Blake & Boogert 2004) at a spectral resolution of R=25,000. The S(9) observations were carried out using a slit width of 0.43". For a description of the data reduction process for these observations see Boogert et al. (2002b).

3. RESULTS

Table 2 summarizes our line detections. We detected H₂ emission from 6 of 29 sources observed: AB Aur, DoAr 21, Elias 29, GSS 30 IRS 1, GV Tau N, and HL Tau. Fluxes, line widths, and centroids were determined by fitting each line individually with a Gaussian profile, which describes the detected lines reasonably well in most cases. In four of the five sources observed from both the IRTF and Gemini, the line fluxes or upper limits from Gemini are smaller than those measured from the IRTF. Since the TEXES slit is larger on the sky at the IRTF, this suggests the H₂ emission may be spatially extended. Figures 3-9 show that the lines are all centered near the stellar velocity suggesting the H₂ is associated with the targets. In all cases, the mid-infrared lines are narrow with observed FWHM near 10 km s⁻¹. Correction for the TEXES instrumental line width of 4-5 km s⁻¹ would give source line widths ~1 km s⁻¹ smaller than observed. For the Keck/NIRSPEC S(9) observations listed in Table 2, removal of the instrumental line broadening would give line widths 3-4 km s⁻¹ narrower than observed. Although our spectra cover ±100 km s⁻¹ from the stellar velocity for the S(2) line, and a similar amount to the red of the S(1) line, we see no evidence for emission at large Doppler shifts. We most often obtain the highest signal-to-noise detections of the S(2) line, where the atmospheric transmission is higher and TEXES is more sensitive.

For emission from optically thin gas, the line flux is given by

$$F = \frac{N_u \times A_{ul} \times h\nu}{4\pi \times d^2}, \quad (1)$$

where N_u is the number of H₂ molecules in the upper state, ν is the line frequency, and d is the distance to the source. The gas mass and temperature enter the equation determining the number of molecules in the upper state, which, under the assumption of LTE at a single temperature, takes the form

$$N_u = \frac{M}{m_{H_2}} \times g_N(2J_u + 1) \frac{hcB}{2kT} e^{-\frac{E_u}{kT}}, \quad (2)$$

where M is the H₂ gas mass, m_{H_2} is the mass of an H₂ molecule, g_N is the nuclear statistical weight (3 or 1 for ortho or para), B is the rotational constant for H₂ taken from Jennings et al. (1984), and E_u is the upper state energy taken from Mandy & Martin (1993).

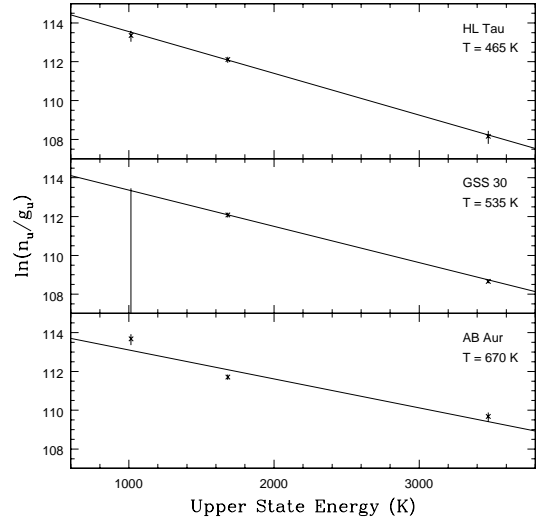


FIG. 1.— Excitation diagrams for the three sources in our sample where we have observations of all three mid-infrared H₂ transitions and detections of at least two. The points are based on Gaussian fits to each of the transitions and are plotted with 1- σ error bars. The overplotted lines show the best-fit single temperature.

In Table 3 we show the derived temperature and mass for the emitting gas in each source based on both single temperature and two-temperature LTE models. Figure 1 shows excitation diagrams for the three sources in our sample where we have observations of all three mid-infrared H₂ transitions and detections of at least two. We assumed optically thin LTE H₂ emission and constructed synthetic spectra for a range of temperatures and masses using the Gaussian line parameters determined from fits to each line individually. We simultaneously fit the synthetic spectra to all of the data for each source, including non-detections, and determined the best fit by minimizing the square of the residuals. The errors listed in Table 3 are 1 σ based on the contour plot of the χ^2 values. We present the results of our best fitting model in the appropriate figures, but defer discussion of the individual sources until the next section.

Tables 4 and 5 list our derived 3 σ line flux upper limits for our IRTF and Gemini observations in the cases where no line was detected. The standard deviation (σ) of the line fluxes was computed by looking at the distribution of values found when assuming a FWHM comparable to our line detections (10 km s⁻¹) and summing over the number of pixels corresponding to that FWHM in regions of the spectrum with comparable atmospheric transmission.

In the case of TW Hya, we used a FWHM of 5.5 km s⁻¹ to compute the line flux upper limits based on the measured width of the (2 σ) S(2) feature. Figure 2 shows observations of TW Hya made during the TEXES/Gemini engineering run in February 2006. There is a hint of a feature near the S(2) position but not a clear detection. Figures 13, 14, 15, and 16 show 3 σ S(1) and S(2) line flux upper limits assuming a FWHM for the lines of 10 km s⁻¹ overplotted on the continuum at the stellar velocity. The gas mass upper limits listed in Tables 4 and 5 were computed under the assumption that the H₂ is in local thermodynamic equilibrium (LTE) and that the emission is optically thin.

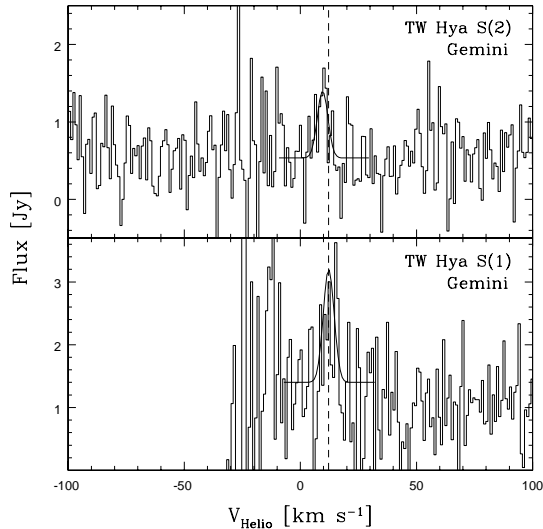


FIG. 2.— TW Hya TEXES/Gemini S(2) and S(1) overplotted with a Gaussian fit to the (2σ) bump near the S(2) position and the 3σ upper limit at S(1). The measured FWHM of 5.5 km s^{-1} for the Gaussian fit at S(2) was assumed to obtain the line flux upper limit at S(1). The S(1) and S(2) upper limits are listed in Table 5. The dashed line indicates the systemic velocity of TW Hya (Kastner et al. 1999).

At the temperatures to which we are sensitive, $T > 200 \text{ K}$, the LTE value of the ortho/para ratio (OPR) is 3, which we assume for our calculations. However, nonequilibrium values of the OPR have been observed in gas at these temperatures. Using *ISO*, Neufeld et al. (1998) derived an OPR of 1.2 towards HH 54 from gas at $T \sim 650 \text{ K}$. They argued that the warm, shocked H_2 gas they observed acquired its OPR at $T < 90 \text{ K}$ and that it has not had time to equilibrate to the LTE value at the higher temperature. Fuente et al. (1999) found an OPR between 1.5 and 2 from 300-700 K gas in a photodissociation region (PDR), which is of interest since the surface layers of the disks we may be observing have similarities with PDRs (Jonkheid et al. 2004). Bitner et al. (2007) claimed that the surface brightness of the H_2 emission observed towards the disk source AB Aur was similar to the Orion bar PDR, lending support to the idea that PDRs and disk surfaces have similar qualities. This was the result of a computation error. In fact, the surface brightness of the H_2 emission from the Orion bar PDR is significantly larger than that of the AB Aur emission. We note that FUV pumping can lead to an apparent OPR in this range even in gas with an equilibrium OPR of 3 due to ortho- H_2 pumping rates being reduced by self-shielding (Sternberg & Neufeld 1999). If the OPR is actually less than 3 in the sources in our sample, a single-temperature fit to our observations would lead us to derive a higher gas temperature because the lowest energy transition we observe is the ortho S(1).

As expected, the upper limits are generally more stringent for the Gemini data than for the IRTF data. The derived 3σ line flux upper limits for our Gemini data are in the range of 10^{-15} to $10^{-14} \text{ ergs s}^{-1} \text{ cm}^{-2}$. Observations with IRS on *Spitzer* of sources with low continuum fluxes give 3σ line flux upper limits of 10^{-16} to $10^{-14} \text{ ergs s}^{-1} \text{ cm}^{-2}$ (Pascucci et al. 2006; Lahuis et al. 2007). The very low upper limits possible with *Spitzer* are for

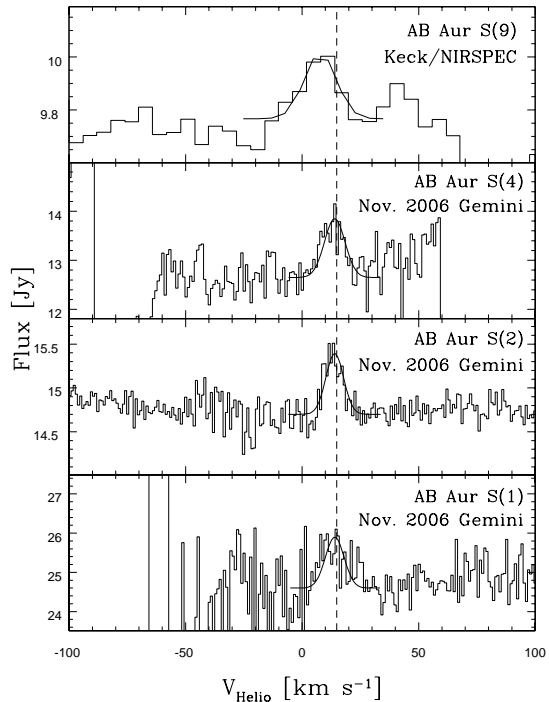


FIG. 3.— AB Aur NIRSPEC/Keck S(9) and TEXES/Gemini S(4), S(2), S(1) data from November 2006 observations overplotted with 2-component model fit. The dashed line shows the stellar velocity (Thi et al. 2001). The increased noise in the S(1) spectrum blueward of the position of the S(1) line is caused by a telluric feature.

sources with continuum fluxes too low to be detected from the ground at the high spectral resolution available with TEXES. In one case where we have a source in common, 49 Cet, our derived upper limits are nearly identical to those obtained with *Spitzer* (Chen et al. 2006). Our upper limits constrain the amount of warm gas with optically thin dust to be below several tens of Earth masses for a temperature of 200 K and less than a few Earth masses at temperatures above 500 K.

4. DISCUSSION

4.1. Individual Sources with H_2 Detections

4.1.1. AB Aur

AB Aur is a Herbig Ae star surrounded by circumstellar material extending to at least $r \sim 450 \text{ AU}$ (Mannings & Sargent 1997). It has a spectral type A0 (Hernández et al. 2004) and is located 144 pc away (van den Ancker et al. 1998). The disk surrounding the $2.4 M_{\odot}$ central star (van den Ancker et al. 1998) has an estimated mass of $0.013 M_{\odot}$ and an inclination of 17_{-3}^{+6} deg as determined by modeling molecular line emission at millimeter wavelengths (Semenov et al. 2005). Observations by Chen & Jura (2003) show that AB Aur is variable in the mid-infrared.

Bitner et al. (2007) described observations of the S(1), S(2), and S(4) H_2 lines using TEXES. A single-temperature LTE model fit to the lines yielded a temperature of $T = 670 \text{ K}$ and $M = 0.52 M_{\oplus}$ for the emitting gas. In this paper, with the addition of observations of the S(9) line, gas at a single temperature no longer fits the data. The two-temperature fit shows that essentially

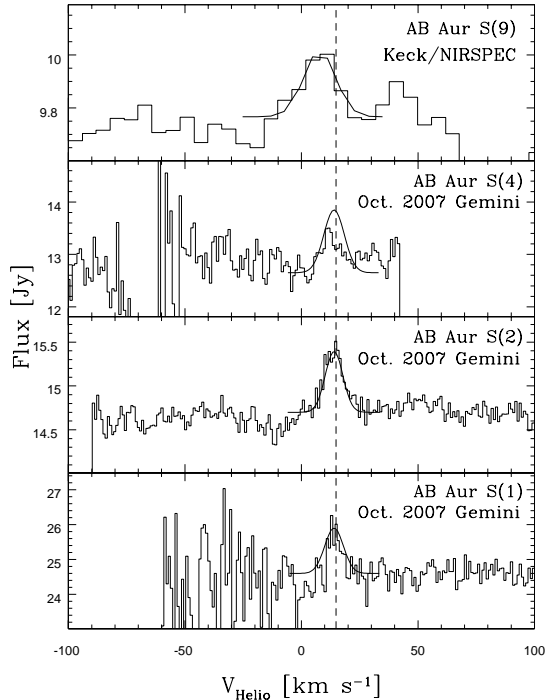


FIG. 4.— AB Aur NIRSPEC/Keck S(9) and TEXES/Gemini S(4), S(2), S(1) data from October 2007 observations overplotted with the 2-component model fit derived using November 2006 data. The S(1) and S(2) lines are consistent with our November 2006 observations, however the S(4) line appears weaker. The dashed line shows the stellar velocity (Thi et al. 2001). The increased noise in the S(1) spectrum blueward of the position of the S(1) line is caused by a telluric feature.

all the S(9) flux comes from a very small amount of gas ($\approx 0.075 M_{\oplus}$) at a temperature likely close to the dust sublimation temperature (Figure 3). It also appears that the high temperature component is slightly blue shifted relative to the gas responsible for the lower energy lines. We observed AB Aur from Gemini on two separate occasions, once during 2006 November and again in 2007 October (Figures 3 and 4). In Figure 4 we show the observations from 2007 overplotted with the two-temperature model based on the 2006 data. While the model is a reasonable fit to the S(1) and S(2) lines, the S(4) line appeared weaker in our 2007 observations. Table 2 shows details of individual Gaussian fits to each of the lines from both years. The S(2) line fluxes are in excellent agreement while the S(1) and S(4) observations show differences. It is possible that the source varied between the two observations. However, the agreement among the two different S(2) observations combined with the fact that we are more sensitive there than at S(1) or S(4) casts doubt on this possibility.

Modeling of the FWHM of the S(2) line profile accounting for Keplerian, instrumental, and thermal broadening suggests that the emission arises near 18 AU in the disk (Bitner et al. 2007). Spatially resolved mid-infrared continuum images at $11.6 \mu\text{m}$ using Michelle on Gemini North by Mariñas et al. (2006) reveal a source size of 17 AU for the emission that remains after the subtraction of a comparison PSF star. Comparison with the passive flared disk model of Dullemond et al. (2001) suggests that, as the disk emerges from the shadow of the

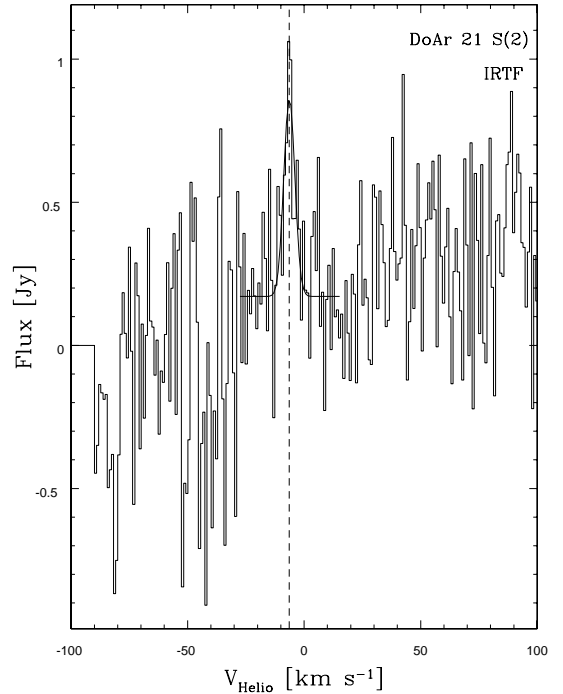


FIG. 5.— DoAr 21 TEXES/IRTF S(2) overplotted with Gaussian fit. The dashed line indicates the systemic velocity of the ρ Oph cloud region (Loren et al. 1990).

inner rim near 10 AU, dust grains in the surface layer are heated by direct stellar radiation, which produces the mid-IR continuum flux. Their derived average dust temperature in this region of ~ 200 K is significantly lower than the gas temperature based on the H₂ observations, implying an additional heating source for the gas. Likely candidates for the source of additional heating are X-ray, UV, and accretion heating. Roberge et al. (2001) detected H₂ in absorption towards AB Aur, probably located in the envelope around the star. They derive a temperature and column density of $T = 212$ K and $N(\text{H}_2) = 6.8 \times 10^{19} \text{ cm}^{-2}$ for the absorbing gas. If we assume the emission is spread evenly over our TEXES beam, the flux in our lines due to this gas is less than $10^{-16} \text{ ergs s}^{-1} \text{ cm}^{-2}$, significantly lower than our detected fluxes. Brittain et al. (2003) detected CO fundamental rovibrational emission from AB Aur and found that the emission was coming from both hot (1540 K) CO in the inner disk rim and cold (70 K) gas farther out in the flared region of the disk. Our derived gas temperature based on the H₂ lines falls between the hot and cold components seen in the CO observations, suggesting we are not seeing the same gas.

4.1.2. DoAr 21

DoAr 21 is located in the ρ Ophiuchus molecular cloud and is classified as a weak-line T Tauri star (Bouvier & Appenzeller 1992). The distance to ρ Ophiuchus remains a source of debate with distance estimates ranging between 119 and 165 pc (Mamajek 2008; Lombardi et al. 2008; Loinard et al. 2008). For the sources in our sample, we adopt the recent distance estimate by Lombardi et al. (2008) of 119 pc. Continuum observations reveal only a slight infrared excess

(Wilkings et al. 2001) and millimeter observations suggest the amount of circumstellar dust is less than $10^{-6} M_{\odot}$ corresponding to a gas mass less than $10^{-4} M_{\odot}$ assuming the standard gas-to-dust ratio (André & Montmerle 1994). Any circumstellar disk around the star is tenuous. Bary et al. (2002) detected narrow, 9 km s^{-1} FWHM, near-infrared $\text{H}_2 v=1-0 \text{ S}(1)$ emission centered at the systemic velocity of DoAr21 and concluded that the line arose from a circumstellar disk within $\sim 110 \text{ AU}$ of the star. Due to the absence of a double-peaked line profile, Bary et al. (2002) concluded that the circumstellar disk in the system has an inclination $< 45^{\circ}$. Bary et al. (2003) calculated that the line emission could be produced by a mass of $2.7 \times 10^{-2} M_{\oplus} \text{ H}_2$ gas in LTE at $T = 1500 \text{ K}$ located in a thin surface layer of the disk. This mass was calculated assuming a distance of 160 pc . Correcting their mass to the 119 pc we assume for DoAr 21, this gas would produce a $\text{S}(2)$ line flux at $12 \mu\text{m}$ of $0.6 \times 10^{-15} \text{ ergs s}^{-1} \text{ cm}^{-2}$, smaller than both our detection from the IRTF and the upper limit based on Gemini data.

We observed DoAr 21 with TEXES on both the IRTF and Gemini North telescopes. From the IRTF, we detected narrow, FWHM $\sim 6 \text{ km s}^{-1}$, $\text{H}_2 \text{ S}(2)$ emission (Figure 5), while the line was not seen in our Gemini observations. Since our slit size on the sky is smaller on Gemini than the IRTF, a plausible explanation for the discrepancy is that the emission is spatially outside our Gemini slit. At the $\text{H}_2 \text{ S}(2)$ setting, our slit widths are $1.4''$ and $0.54''$ on the IRTF and Gemini respectively. At an adopted distance of 119 pc to DoAr 21, these slit widths translate to physical distances from the central source of 83 AU and 32 AU . Our data suggest that the observed H_2 emission arises outside of the inner 32 AU around DoAr 21. The rovibrational emission seen in DoAr 21 (Bary et al. 2002) was observed using the Phoenix spectrometer (Hinkle et al. 1998) on the NOAO 4-meter telescope on Kitt Peak with a seeing-limited slit width, the same as TEXES at the IRTF. If our observations probe the same gas, this is consistent with the possibility that the emitting region is outside of the inner $\sim 30 \text{ AU}$.

4.1.3. Elias 29

Elias 29 is a class I protostar located in the ρ Ophiuchus molecular cloud. Along with several nearby protostars, it is located along a dense ridgeline structure seen in $\text{HCO}^+ 3-2$ emission (Boogert et al. 2002a). The central source is surrounded by a circumstellar disk and a remnant envelope several times more massive than the disk (Lommen et al. 2008). Modeling of the spectral energy distribution (Boogert et al. 2002a) constrains the disk size to $\sim 500 \text{ AU}$ with an inclination less than 60° and mass of $0.012 M_{\odot}$.

Using the *Infrared Space Observatory (ISO)* Short Wavelength Spectrometer, Ceccarelli et al. (2002) saw evidence for a disk around Elias 29 with a superheated surface layer and mass similar to disks around Herbig AeBe stars. These authors suggested that Elias 29 may actually be a deeply embedded Herbig AeBe star. Boogert et al. (2002a) also suggested Elias 29 might be a heavily extinguished T Tauri or Herbig AeBe star. Elias 29 drives a bipolar CO outflow (Bontemps et al. 1996) with velocities approaching $\sim 80 \text{ km s}^{-1}$ (Boogert et al.

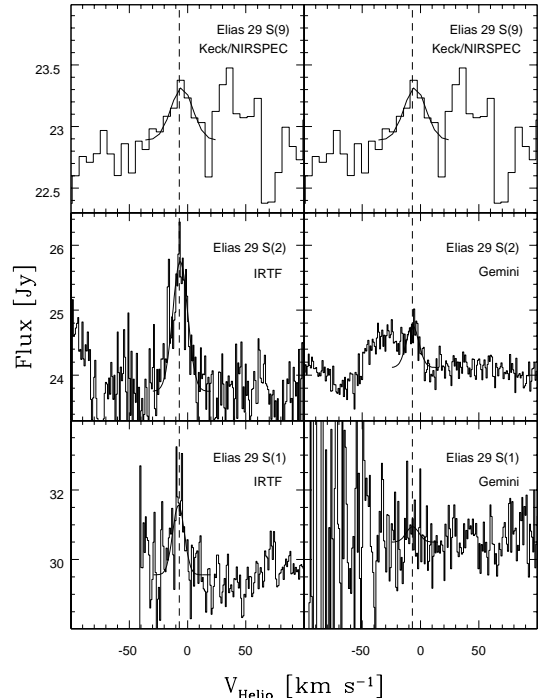


FIG. 6.— Elias 29 NIRSPEC/Keck S(9), TEXES/IRTF S(2), S(1), and TEXES/Gemini S(2), S(1) overplotted with 1-component model fit. The dashed line indicates the systemic velocity of Elias 29 (Boogert et al. 2002a). The continuum has been scaled to agree with the *ISO* SWS measurement. The bump redward of the S(9) feature is due to telluric contamination. Poor telluric division of a water feature is apparent on the blue side of the Gemini S(2) line.

2002a). Knotty $\text{H}_2 1-0 \text{ S}(1)$ emission suggests the presence of a precessing jet interacting with the surrounding medium and clearing the protostellar envelope (Ybarra et al. 2006).

We used TEXES on the IRTF in 2003 June and on Gemini North in 2006 July to observe Elias 29 at the $\text{H}_2 \text{ S}(1)$ and $\text{S}(2)$ settings. We obtained observations of the $\text{H}_2 \text{ S}(9)$ line taken with Keck/NIRSPEC during several runs between 2000 and 2005. The data are shown overplotted with a single temperature LTE model fit in Figure 6. The Gemini spectrum shows poor telluric division on the blue side of the S(2) line. A telluric water feature at this velocity apparently was not well corrected. The results of the single temperature LTE model fits to the data are listed in Table 3. The data are well fit by emission from less than $1 M_{\oplus}$ of gas at $T \sim 1000 \text{ K}$. The S(2) line was > 3 times stronger in our IRTF observations compared to Gemini and the S(1) line is clearly detected in our IRTF observations but not seen from Gemini. There are two possible explanations for these discrepancies. Either the H_2 line flux actually changed between our observations from the IRTF and Gemini, or the emission is spatially extended and our wider slit on the IRTF took in more of the line flux. We saw no evidence of spatially resolved H_2 emission along the slit of our Gemini observations at scales of 0.4 arcsec ($\sim 25 \text{ AU}$ in radius at 119 pc). The continuum level did not vary significantly between our IRTF and Gemini observations.

4.1.4. GSS 30 IRS 1

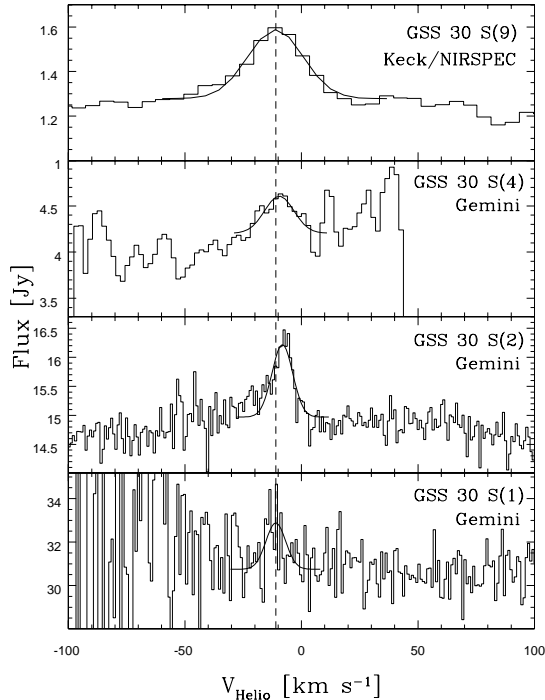


FIG. 7.— GSS 30 NIRSPEC/Keck S(9) and TEXES/Gemini S(4), S(2), S(1) overplotted with 2-component model fit. The dashed line shows the systemic velocity (Pontoppidan et al. 2002). The continuum has been scaled to agree with the *Spitzer* IRS measurement.

GSS 30 IRS 1 is a class I source (Wilkings et al. 1989) in the ρ Ophiuchus molecular cloud. Near-infrared polarimetry by Chrysostomou et al. (1997) suggests that the source is surrounded by a large flattened dusty envelope and a more compact circumstellar disk. Modeling of near-infrared polarimetry data suggests the disk has an inclination of $\sim 65^\circ$, i.e. closer to edge-on (Chrysostomou et al. 1996). Nearby molecular outflow activity has been observed but is not clearly associated with GSS 30 IRS1 itself. Tamura et al. (1990) observed high velocity millimeter CO emission to the south of GSS 30 IRS1 that is likely associated with the nearby VLA 1623 jet (André et al. 1990).

Pontoppidan et al. (2002) described observations of fundamental rovibrational CO emission at $4.7 \mu\text{m}$. The lines are unresolved at $R = 5000$ and are spatially extended up to 320 AU from the central source. The authors proposed that the line emission arises from post-shocked gas from the inner region of the circumstellar disk, which is then scattered into our line of sight by the surrounding envelope. The lines are consistent with 1-100 M_\oplus of gas in LTE at $T = 515$ K with a spatial extent of ~ 20 -100 AU.

Our pure rotational H₂ data cannot be fit by a LTE single temperature/mass model, but is fit reasonably well with a two component model (Figure 7). Using a two component fit, we find a temperature for the low J lines nearly identical to Pontoppidan et al. (2002). The S(9) emission arises in a small amount of hot gas, significantly hotter at 3300 K than the dust evaporation temperature, and has a broader line width than the other H₂ lines. Because such hot gas temperatures are

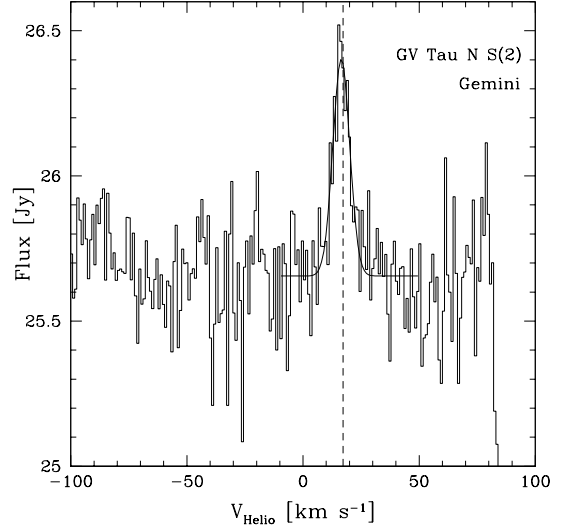


FIG. 8.— GV Tau N TEXES/Gemini S(2) overplotted with Gaussian fit. The dashed line indicates the systemic velocity of the GV Tau system (Hogerheijde et al. 1998).

only effectively constrained by the S(9) line, our determination of this temperature is more uncertain. Since the H₂ molecule may form in a high rotational level (Wagenblast 1992), this apparent high temperature, if valid, may be due to H₂ formation pumping. As noted by Pontoppidan et al. (2002), the intrinsic line widths are expected to be $\sim 10 \text{ km s}^{-1}$ or larger in the case where a dissociating accretion shock is responsible for the emission. The width of the low J pure rotational H₂ lines are consistent with this model. The hot gas, however, is likely located in a separate location.

4.1.5. GV Tau N

GV Tau is a pre-main-sequence binary system in the L1524 molecular cloud. The two components are separated by $1.2''$ (170 AU at 140 pc) (Leinert & Haas 1989). The southern component is optically visible while GV Tau N is heavily extinguished. Near-infrared imaging and optical polarimetry show that the system is surrounded by a flattened, edge-on circumbinary envelope out to ~ 1000 -1500 AU (Ménard et al. 1993). GV Tau N shows near-infrared variability on timescales as short as a month, which has been attributed to clumpiness in the surrounding material (Leinert et al. 2001). The GV Tau system has a spectral energy distribution rising through the mid-infrared leading to its classification as a class I source, however, millimeter observations by Hogerheijde et al. (1998) suggest that most of the envelope has disappeared. GV Tau N appears to be driving a Herbig-Haro outflow (Devine et al. 1999). Gibb et al. (2007) reported the detection of near-infrared absorption lines due to CO, HCN, and C₂H₂ toward GV Tau S and derived a CO rotational temperature of ~ 200 K, suggesting the observed gas is in the inner region of a circumstellar disk. Doppmann et al. (2008) observed HCN, C₂H₂, and CO absorption towards GV Tau N but did not detect molecular absorption towards GV Tau S. Mid-infrared observations with TEXES on Gemini in 2006 November also showed HCN absorption towards GV Tau N but not GV Tau S (Najita et al., in preparation).

We observed GV Tau N at the S(2) setting (Figure 8)

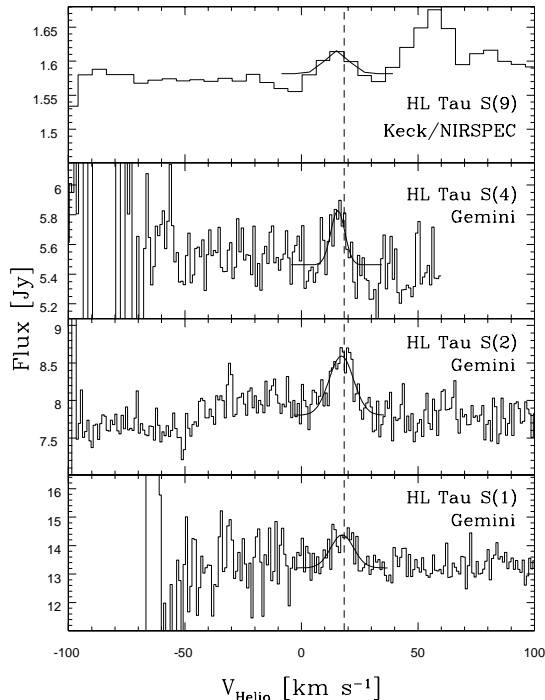


FIG. 9.— HL Tau NIRSPEC/Keck S(9) and TEXES/Gemini S(4), S(2), S(1) overplotted with 2-component fit. The dashed line shows the stellar velocity (White & Hillenbrand 2004). The continuum has been scaled to agree with the *ISO* SWS measurement. The bump redward of the very weak S(9) feature is due to telluric contamination.

from Gemini and detected emission at a flux level and line width consistent with other detections in our sample. The detection of just a single line precludes an estimate of the temperature and mass of the emitting gas. Doppmann et al. (2008) observed near-infrared H_2 emission from GV Tau N in the $v=1-0$ S(2) and $v=1-0$ S(0) lines. The line centroids are consistent with our mid-infrared S(2) detection and with the systemic velocity of GV Tau. The $v=1-0$ S(2) line emission is stronger than the $v=1-0$ S(0) by a factor that is consistent with the shock excitation seen in classical T Tauri stars by Beck et al. (2008).

4.1.6. HL Tau

The young stellar object, HL Tau, is in an intermediate stage between an embedded class I protostar and an optically visible T Tauri star (Pyo et al. 2006). It is surrounded by a $0.05-0.07 M_{\odot}$ circumstellar disk with an outer radius of 90-160 AU (Mundy et al. 1996) inclined by 66-71 degrees from face-on (Lucas et al. 2004). Molecular carbon absorption suggests the presence of an infalling envelope (Grasdalen et al. 1989). A collimated jet is seen from HL Tau in [Fe II] $1.6 \mu\text{m}$ emission surrounded by a wide-angled wind, which produces shocked near-infrared H_2 emission (Takami et al. 2007). Spatially resolved observations by Beck et al. (2008) with NIFS on Gemini North confirm that the near-infrared H_2 $v=1-0$ S(1) emission is consistent with the location of the jet associated with the system. Nearly half of the NIR H_2 emission seen by Beck et al. (2008) is spatially coincident with the continuum. If the spatial distribution of the mid-infrared H_2 emission is the same as the near-infrared

H_2 emission, our observed emission lines may also originate in circumstellar gas shocked by the jet. Broad near-infrared CO emission from the hot ($T \sim 1500$ K) inner disk along with narrow CO absorption likely originating in the outer flared disk are observed from HL Tau (Brittain et al. 2005). Brittain et al. (2005) estimated that the emission arises from CO with a column density of $4 \times 10^{16} \text{ cm}^{-2}$ in a region between 0.066 AU and 0.53 AU. This translates to $\sim 10^{-4} M_{\oplus}$ of H_2 at 1500 K, which would produce pure rotational mid-infrared H_2 emission at levels $\sim 10^{-18} \text{ ergs s}^{-1} \text{ cm}^{-2}$, well below our detection limits. This combined with the average FWHM of the CO lines observed by Brittain et al. (2005) (45 km s^{-1}) makes clear that our observations are probing gas at larger radii. From the IRTF, we detected emission in the H_2 S(2) line, while from Gemini we detected H_2 S(1), S(2), and S(4) emission. A single temperature LTE model comprised of $\sim 1 M_{\oplus}$ of 465 K gas fits the observations well (Figure 9). The emission lines are all narrow with FWHM near 10 km s^{-1} .

4.2. Putting TEXES Results into the Context of Other Circumstellar Gas Observations

Emission has been detected in the near-infrared $v=1-0$ S(1) transition of H_2 from several T Tauri stars (Bary et al. 2003). The detected emission shares similar characteristics with our observations of the mid-infrared H_2 lines. In both cases the lines are narrow and centered at the systemic velocity of the star. The observed near-infrared H_2 lines all have FWHM $\sim 10 \text{ km s}^{-1}$, suggesting that the emission arises 10-50 AU away from the star and is possibly the result of excitation by UV or X-rays. The spatially resolved observations of $v=1-0$ S(1) H_2 emission from the circumstellar environments of classical T Tauri stars by Beck et al. (2008) are most consistent with shock excited emission from outflows rather than UV or X-ray excitation.

Three of the sources with detected near-infrared H_2 emission in the Bary et al. (2003) sample were also observed as part of our TEXES H_2 mid-infrared survey. Two of those sources, GG Tau and LkCa 15, do not have detectable levels of mid-infrared H_2 emission while the other, DoAr 21, was detected in the S(2) line in our IRTF observations but not when re-observed from Gemini. Bary et al. (2003) computed the amount of H_2 gas required to produce the observed emission in these sources under the assumption of LTE at $T=1500$ K. Based on their derived gas masses for these three sources, we computed the amount of emission we would see in the mid-infrared H_2 S(1) and S(2) lines. For GG Tau and LkCa 15, the predicted line fluxes are all less than a few times $10^{-16} \text{ ergs s}^{-1} \text{ cm}^{-2}$ consistent with our derived upper limits. In the case of DoAr 21, the predicted line fluxes are less than $10^{-15} \text{ ergs s}^{-1} \text{ cm}^{-2}$, smaller than both our non-detections from Gemini and the detected S(2) line flux observed with the IRTF from DoAr 21.

CO fundamental rovibrational emission near $4.6 \mu\text{m}$ is detected in many T Tauri stars (Najita et al. 2003) and Herbig AeBe stars (Blake & Boogert 2004). The A -values for the CO fundamental lines are much larger than those of the pure rotational mid-infrared H_2 lines and so, assuming LTE, the CO lines are more sensitive to small column densities of gas. The lines are broad and centrally

peaked with FWHM of 50-100 km s⁻¹, suggesting the emission arises from $\lesssim 0.1$ AU to 1-2 AU (Najita et al. 2007a). The CO near-infrared observations typically reveal temperatures of 1000-1500 K and CO column densities of $\sim 10^{18}$ cm⁻² (Najita et al. 2007a). Assuming the CO fundamental emission arises from 0.1-2 AU with a CO column density of 10^{18} cm⁻² and a CO/H₂ ratio of 2.7×10^{-4} (Lacy et al. 1994) gives a mass of H₂ in this region of $\sim 10^{-2}$ M_⊙. The line fluxes in the mid-infrared H₂ lines from such gas at T = 1000 K are less than 10^{-15} ergs s⁻¹ cm⁻², smaller than our detection limits. The additional line broadening due to the larger rotation speeds in this part of the disk would further decrease the chances of this gas being seen in our high resolution mid-infrared H₂ observations. HD 141569 is a unique source among those with observed near-infrared CO emission in that the emission arises from gas at a much cooler temperature (190 K) and at a location $\gtrsim 17$ AU in the disk (Brittain et al. 2003). Brittain et al. (2003) derived a mass for the emitting CO gas of 10^{19} g ($\sim 10^{-9}$ M_⊙). For a rotational temperature of 190 K, assuming the CO/H₂ ratio derived by Lacy et al. (1994), the expected mid-infrared H₂ line fluxes are smaller than 10^{-20} ergs s⁻¹ cm⁻², consistent with our non-detections.

4.3. Location of Emitting H₂ Gas and Possible Excitation Mechanism

The six stars with detected H₂ emission all have narrow, spectrally resolved line widths between 7 and 15 km s⁻¹. Added to the fact that the line fluxes are all similar and that the lines are centered at the stellar velocity, this suggests that the excitation mechanism is similar in each case. If the emission originates in a circumstellar disk, our spectrally resolved lines allow for the determination of the approximate emission radius. We created simple models for the line widths originating from a Keplerian disk that contributes equally at all radii within some annulus and convolved these line profiles with the TEXES instrumental profile and thermal broadening appropriate for gas at T = 500 K, roughly the temperature derived from our observations. For a star of one solar mass with a disk inclination angle of 45°, the range of line widths detected in our sample corresponds to emission from disk radii between 10 and 50 AU.

In all cases, our observations show the emission is spatially unresolved along the slit of our Gemini observations at scales of 0.4 arcsec and coincident with the source continuum. This combined with the fact that the lines are spectrally resolved with FWHM ~ 10 km s⁻¹ suggests that we are not seeing emission from an extended envelope surrounding the source, which would produce narrow, spectrally unresolved lines. Furthermore, it is unlikely we are seeing the results of shocks associated with jets and outflows commonly seen near young stars, as that would produce broader lines with some displacement from the stellar velocity.

However, the spatially resolved ($\sim 0.1''$) observations of near-infrared H₂ emission from the circumstellar environments of six classical T Tauri stars by Beck et al. (2008) demonstrate that we cannot rule out shocked emission as the source of our observed mid-infrared lines in all cases. One source we share with Beck et al. (2008) is HL Tau. Beck et al. (2008) concluded that their spatially

resolved observations of the near-infrared $v=1-0$ S(1) H₂ line from HL Tau are consistent with the location of the jet in the system. In addition, nearly half of the observed H₂ emission from HL Tau is spatially coincident with the continuum and the line centroid is within 10 km s⁻¹ of the stellar velocity. Assuming the spatial position of the near-infrared and mid-infrared H₂ emission is the same, this suggests that the emission we observed may also arise in shock excited circumstellar gas. However, there is a notable difference in the overall results of the spatially resolved, near-infrared H₂ observations by Beck et al. (2008) and our mid-infrared H₂ observations. In half of the six stars observed, the near-infrared line centroids differed by more than 10 km s⁻¹ from the stellar velocity whereas in our sample, all of the H₂ line centroids are within a few km s⁻¹ of the stellar velocity.

The results of spectral energy distribution modeling of the dust temperature in the surface layer of a disk around a typical T Tauri star show that the dust temperature is $\lesssim 200$ K at disk radii larger than 10 AU where our H₂ emission arises (Chiang & Goldreich 1997). Stellar heating of dust grains in the disk atmosphere coupled to the gas temperature through gas/grain collisions is insufficient to explain the high gas temperatures derived from our observations. Carmona et al. (2008a) computed the expected emission in the H₂ S(1) and S(2) lines from the optically thick, two-layer disk model of Chiang & Goldreich (1997) in which dust in the disk surface layer absorbs stellar radiation and heats the gas. They found that the amount of gas in the warm surface layer of the disk is less than a few Earth masses. At a distance of 140 pc, this leads to predicted mid-IR H₂ line fluxes of $10^{-17} - 10^{-16}$ ergs s⁻¹ cm⁻², much lower than both the levels of our detections and our upper limits. Carmona et al. (2008a) pointed out that the two-layer approximation to the disk structure leaves out details that could significantly contribute to H₂ emission. They found that departures from thermal coupling between gas and dust in the disk surface layer as well as larger than interstellar gas-to-dust ratios can lead to detectable levels of H₂ emission. Two plausible mechanisms for additional gas heating in the surface layers of disks are accretion shocks due to infalling matter onto the disk and X-ray/UV irradiation. That accretion onto the disk may play a role in exciting H₂ emission is consistent with the preferential detection of H₂ emission from the class I sources in our sample, which possess a surrounding envelope of material in addition to a disk.

Neufeld & Hollenbach (1994) have calculated the physical and chemical structure of shocks resulting from accretion onto a circumstellar disk, but they did not publish the strength of the pure rotational H₂ lines from their model. However, we have reviewed the results of unpublished models from their study to determine the parameters that would produce H₂ emission at the levels detected in our observations. Neufeld & Hollenbach (1994) only considered preshock densities above 3×10^7 cm⁻³. However, below this density, the fraction of the total cooling from H₂ emission increases. A shock with a preshock density of 10^6 cm⁻³ striking the disk at 5 km s⁻¹ at 30 AU implies an accretion rate of 5×10^{-8} M_⊙ yr⁻¹. The resulting emission in the S(1), S(2), and S(4) H₂ lines is $\sim 10^{-6}$ L_⊙. This accretion rate is similar

to the measured rates for the sources where we have detected H_2 emission and these line luminosities are only slightly lower than our observations. One way to increase the H_2 cooling in the model is to suppress the cooling in H_2O lines in the shock by assuming that H_2O is frozen out as water ice in the preshock gas. It is plausible that the H_2O would be frozen out for the 5 km s^{-1} shocks since they are slow enough that they would not return the H_2O to the gas phase. If this were the case, the luminosity in our H_2 lines would increase by an order of magnitude to about $10^{-5} L_\odot$. The line luminosities detected in our sample range from 10^{-6} to $10^{-5} L_\odot$ suggesting that shock heating due to accretion onto a disk is a plausible excitation mechanism. Additional details including predicted CO line strengths can be found in the Appendix.

Nomura et al. (2007) modeled the molecular hydrogen emission from a disk surrounding a typical T Tauri star, taking into account the heating of gas by X-ray and UV irradiation from the central star. The resulting gas temperature in the surface layer of the disk is much higher than the dust temperature. X-ray heating dominates in the inner region and surface layer of the disk. At 10 AU, the disk surface temperature reaches over 1000 K. Even at 100 AU, the temperature in the disk surface layer reaches 200 K. These temperatures combined with the fact that the gas is hotter than the dust creates favorable conditions for the production of mid-infrared H_2 emission lines. The predicted line fluxes derived by Nomura et al. (2007) appropriate for TW Hya vary depending on the adopted dust size distribution. The quoted line fluxes at our wavelengths are $4.4 - 9.9 \times 10^{-15} \text{ ergs s}^{-1} \text{ cm}^{-2}$ at S(1), $1.7 - 4.8 \times 10^{-15} \text{ ergs s}^{-1} \text{ cm}^{-2}$ at S(2), and $0.4 - 8.8 \times 10^{-15} \text{ ergs s}^{-1} \text{ cm}^{-2}$ at S(4). At distances more typical of the sources in our sample, these fluxes are $\sim 10^{-16} \text{ ergs s}^{-1} \text{ cm}^{-2}$. In the sources where we detect line emission, the derived line fluxes are all larger, typically 10^{-15} - $10^{-14} \text{ ergs s}^{-1} \text{ cm}^{-2}$. Gorti & Hollenbach (2008) have also modeled line emission from the upper layers of optically thick disks. Their predicted H_2 emission line luminosities are 10^{-6} to $10^{-5} L_\odot$ and are consistent with the range of detected emission in our sample. The difference in the predictions of the two models shows that the modeling is very sensitive to the input parameters. The FUV flux assumed by Gorti & Hollenbach (2008) in their standard model is five times higher and the X-ray flux is three times larger than the values used by Nomura et al. (2007) which leads to the higher predicted H_2 line fluxes.

In Figure 10, we present a plot of our H_2 detections and upper limits versus the X-ray luminosity of the stars in our sample. If high X-ray luminosities were responsible for heating the gas in disks above the dust temperature to produce detectable H_2 emission, we should see a correlation between detected H_2 emission and X-ray luminosity. As seen in Figure 10, such a correlation is not apparent in our data. In several cases, we detect H_2 emission from sources at the faint end of the distribution of X-ray luminosities, while we did not detect H_2 emission from the most X-ray luminous stars in our sample. It is worth noting that X-ray flux has been observed to vary by more than an order of magnitude on timescales of days (Kastner et al. 1999). To definitively test for ob-

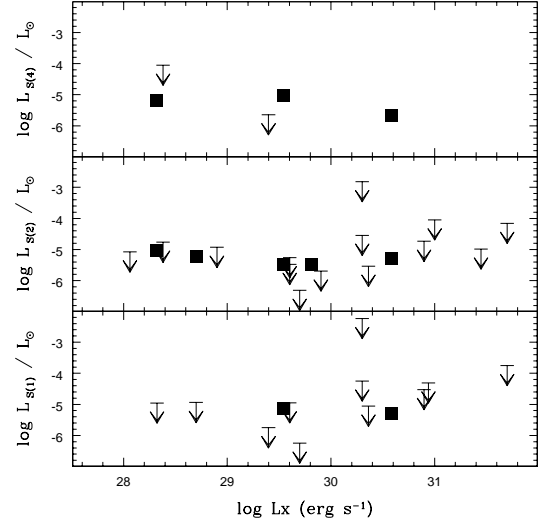


FIG. 10.— Gemini H_2 line luminosities vs. X-ray luminosity of each source. The solid points are H_2 detections and the arrows represent upper limits. No correlation between the presence of H_2 emission and X-ray luminosity is apparent.

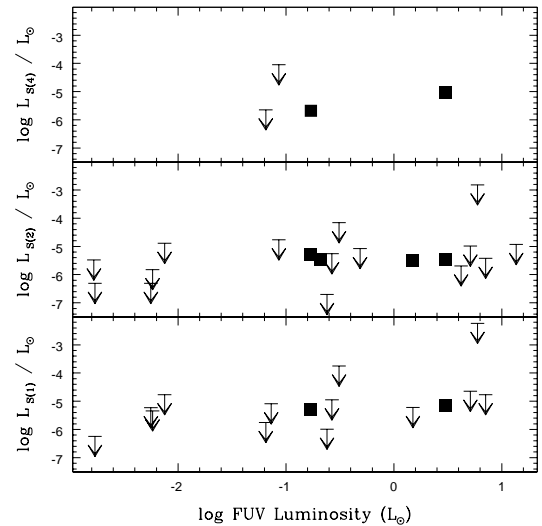


FIG. 11.— Gemini H_2 line luminosities vs. FUV luminosity of each source. The solid points are H_2 detections and the arrows represent upper limits. There is a hint of a correlation between FUV luminosity and detected H_2 emission for the small sample of S(4) data points, however there is no clear overall correlation.

servational evidence of a correlation between X-ray flux and H_2 emission requires a series of coordinated observations. UV irradiation of the disk from the central star may also contribute to heating the gas in the disk, leading to detectable levels of H_2 emission. We plot H_2 line luminosity versus FUV luminosity in Figure 11 and find no clear correlation, however. Since accretion heating may play a role in producing H_2 emission, we plot H_2 line luminosity versus accretion rate in Figure 12 to look for a correlation. The sources in our sample with detected H_2 emission are located in the middle of the range of accretion rates, showing no clear correlation. Since the dynamic range separating our H_2 detections from the non-detections is not very large, the lack of a correlation

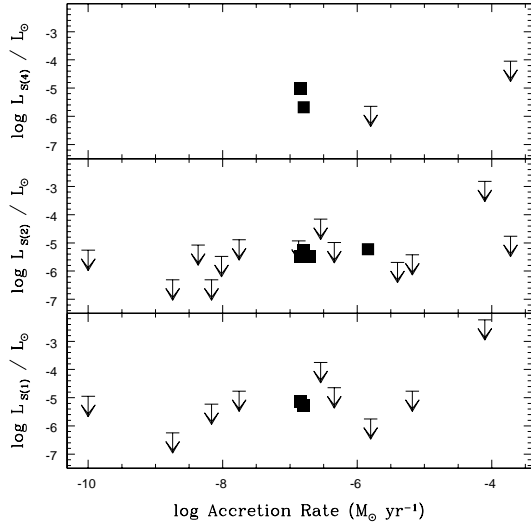


FIG. 12.— Gemini H₂ line luminosities vs. accretion rate measured in each source. The solid points are H₂ detections and the arrows represent upper limits. The sources with detected H₂ emission fall in the middle of the range of accretion rates.

between L_x , L_{FUV} , \dot{M} and detected H₂ does not conclusively rule out the possible importance of X-ray, UV, and accretion heating in producing H₂ emission. We also searched for a correlation between H₂ emission and mass, age, and inclination but found none.

5. CONCLUSIONS

We have carried out a survey for pure rotational H₂ emission from the circumstellar environments surrounding a sample of 29 stars with disks and detected emission from 6. In the case of non-detections, our upper limits constrain the amount of $T > 500$ K gas in the surface layers of the circumstellar disks to be less than a few Earth masses. Several objects in our survey have transition object SEDs implying the presence of an optically thin, dust-depleted inner disk: DoAr 21, GM Aur, HD 141569, and LkCa 15. Among these sources, only DoAr 21 shows H₂ emission and it appears to be far from the star. One possible explanation for transitional SEDs is grain growth (Strom et al. 1989; Dullemond & Dominik 2005) whereby the inner disk becomes optically thin yet remains gas rich. This gas could be heated through accretion as well as X-ray and UV heating. GM Aur is of particular interest since it has an accretion rate ($\sim 10^{-8} M_{\odot} \text{ yr}^{-1}$) similar to typical CTTS accretion rates so should have as much gas in the inner disk as a typical CTTS. If grain growth is responsible for the transitional SEDs of these sources, the available heating mechanisms are insufficient to produce detectable H₂ line emission. Alternatively, grain growth may not be a good explanation for a transition object SED, as suggested by other demographic data (Najita et al. 2007b).

In all cases, the detected emission lines are narrow and centered at the stellar velocity. The narrow range of line widths, FWHM between 7 and 15 km s⁻¹, along with the fact that the line fluxes are all similar, suggests that the mechanism for exciting the emission may be the same in each case. Four of the six targets with detected emission are class I sources that show evidence for surrounding material in an envelope in addition to a circumstellar

disk. It is possible, and likely in the case of HL Tau, that the H₂ emission we observe is a result of gas in the circumstellar envelope being shock heated by an outflow. However, the fact that all of the H₂ line centroids in our sample are within a few km s⁻¹ of the stellar velocity argues against this being the case for all of our detections.

Under the assumption of emission from a disk in Keplerian rotation, the narrow line widths imply that the emission arises at disk radii from 10-50 AU. At such large disk radii, additional heating of the gas besides heating due to collisions with dust grains is required to explain the temperatures derived from our H₂ observations. Both X-ray/UV irradiation of the disk surface layer and accretion shocks resulting from matter infall onto the disk are plausible candidates. With the exception of DoAr 21, all of the sources where we detect H₂ emission possess both a circumstellar disk and a surrounding envelope of material. This lends support to the possibility that the H₂ emission we observed may be the result of shocks in the disk due to infalling material.

Models of molecular hydrogen emission from disks that assume sufficient levels of stellar X-ray and UV irradiation (Gorti & Hollenbach 2008) predict line fluxes that are consistent with our observations. In contrast, models which assume smaller values of stellar UV and X-ray irradiation (Nomura et al. 2007) produce weaker H₂ emission than observed in our sample. We looked for evidence of a correlation between X-ray/UV luminosity and the presence of H₂ emission but found none. We note that the X-ray and UV luminosities used for the purpose of searching for a correlation with H₂ emission were not measured at the same time. To definitively test for a correlation between X-ray/UV luminosity and the presence of H₂ emission will require a series of coordinated observations.

We thank the Gemini staff, and John White in particular, for their support of TEXES observations on Gemini North. We are also grateful to the anonymous referee for helpful comments on this manuscript. The development of TEXES was supported by grants from the NSF and the NASA/USRA SOFIA project. Modification of TEXES for use on Gemini was supported by Gemini Observatory. Observations with TEXES were supported by NSF grant AST-0607312. MJR acknowledges support from NSF grant AST-0708074 and NASA grant NNG04GG92G. Some of the data presented herein were obtained at the W.M. Keck Observatory, which is operated as a scientific partnership among the California Institute of Technology, the University of California and the National Aeronautics and Space Administration. The Observatory was made possible by the generous financial support of the W.M. Keck Foundation. This work is based on observations obtained at the Gemini Observatory, which is operated by the Association of Universities for Research in Astronomy, Inc., under a cooperative agreement with the NSF on behalf of the Gemini partnership: the National Science Foundation (United States), the Particle Physics and Astronomy Research Council (United Kingdom), the National Research Council (Canada), CONICYT (Chile), the Australian Research Council (Australia), CNPq (Brazil) and CONICET (Argentina).

REFERENCES

- Alencar, S.H.P., & Batalha, C. 2002, *ApJ*, 571, 378
- André, Ph., Martín-Pintado, J., Despois, D., & Montmerle, T. 1990, *A&A*, 236, 180
- André, Ph., & Montmerle, T. 1994, *ApJ*, 420, 837
- Bary, J.S., Weintraub, D.A., & Kastner, J.H. 2002, *ApJ*, 576, L73
- Bary, J.S., Weintraub, D.A., & Kastner, J.H. 2003, *ApJ*, 586, 1136
- Beck, T.L., McGregor, P.J., Takami, M., & Pyo, T.-S. 2008, *ApJ*, 676, 472
- Berghöfer, T.W., Schmitt, J.H.M.M., & Cassinelli, J.P. 1996, *A&AS*, 118, 481
- Bergin, E., et al. 2004, *ApJ*, 614, L133
- Berrilli, F., Corciulo, G., Ingrassio, G., Lorenzetti, D., Nisini, B., & Strafella, F. 1992, *ApJ*, 398, 254
- Bitner, M.A., Richter, M.J., Lacy, J.H., Greathouse, T.K., Jaffe, D.T., & Blake, G.A. 2007, *ApJ*, 661, L69
- Blake, G.A., & Boogert, A.C.A. 2004, *ApJ*, 606, L73
- Bontemps, S., André, P., Tereby, S., & Cabrit, S. 1996, *A&A*, 311, 858
- Boogert, A.C.A., Hogerheijde, M.R., Ceccarelli, C., Tielens, A.G.G.M., van Dishoeck, E.F., Blake, G.A., Latter, W.B., & Motte, F. 2002a, *ApJ*, 570, 708
- Boogert, A.C.A., Blake, G.A., & Tielens, A.G.G.M. 2002b, *ApJ*, 577, 271
- Bouvier, J. & Appenzeller, I. 1992, *A&AS*, 92, 481
- Brittain, S.D., Rettig, T.W., Simon, T., Kulesa, C., DiSanti, M.A., & Dello Russo, N. 2003, *ApJ*, 588, 535
- Brittain, S.D., Rettig, T.W., Simon, T., & Kulesa, C. 2005, *ApJ*, 626, 283
- Burton, M.G., Hollenbach, D.J., & Tielens, A.G.G. 1992, *ApJ*, 399, 563
- Calvet, N., Muzerolle, J., Briceño, C., Hernández, J., Hartmann, L., Saucedo, J.L., & Gordon, K.D. 2004, *AJ*, 128, 1294
- Carkner, L., Kozak, J.A., & Feigelson, E.D. 1998, *ApJ*, 116, 1933
- Carmona, A., et al. 2008a, *A&A*, 477, 839
- Carmona, A., van den Ancker, M.E., Henning, Th., Goto, M., Fedele, D., & Stecklum, B. 2008b, *A&A*, 478, 795
- Carr, J.S., Tokunaga, A.T., & Najita, J. 2004, *ApJ*, 603, 213
- Carr, J.S., Najita, J. 2008, *Science*, 319, 1504
- Ceccarelli, C., Boogert, A.C.A., Tielens, A.G.G.M., Caux, E., Hogerheijde, M.R., & Parise, B. 2002, *A&A*, 395, 863
- Cernis, K. 1990, *Ap&SS*, 166, 315
- Chavarría, K.C., de Lara, E., Finkenzeller, U., Mendoza, E.E., & Ocegueda, J. 1988, *A&A*, 197, 151
- Chen, C.H., & Jura, M. 2003, *ApJ*, 591, 267
- Chen, C.H., et al. 2006, *ApJS*, 166, 351
- Chiang, E.I., & Goldreich, P. 1997, *ApJ*, 490, 368
- Chrysostomou, A., Clark, S.G., Hough, J.H., Gledhill, T.M., McCall, A., & Tamura, M. 1996, *MNRAS*, 278, 449
- Chrysostomou, A., Ménard, F., Gledhill, T.M., Clark, S., Hough, J.H., McCall, A., & Motohide, T. 1997, *MNRAS*, 285, 750
- de Geus, E.J., de Zeeuw, P.T., & Lub, J. 1989, *A&A*, 216, 44
- Devine, D., Reipurth, B., Bally, J. & Balonek, T.J. 1999, *AJ*, 117, 2931
- Dolan, C.J., & Mathieu, R.D. 2001, *AJ*, 121, 2124
- Doppmann, G.W., Najita, J.R., & Carr, J.S. 2008, *ApJ*, submitted
- Draine, B.T. 1980, *ApJ*, 241, 1021
- Draine, B.T., Roberge, W.G., & Dalgarno, A. 1983, *ApJ*, 264, 485
- Draine, B.T., & Roberge, W.G. 1984, *ApJ*, 282, 491
- Dullemond, C.P., Dominik, D. & Natta, A. 2001, *ApJ*, 560, 957
- Dullemond, C.P., & Dominik, C. 2005, *A&A*, 434, 971
- Edwards, S., Fischer, W., Kwan, J., Hillenbrand, L., & Dupree, A.K. 2003, *ApJ*, 599, L41
- Elias, J.H. 1978, *ApJ*, 224, 857
- Espallat, C., Calvet, N., D'Alessio, O., Hernandez, J., Qi, C., Hartmann, L., Furlan, E., & Watson, D.M. 2007, *ApJ*, 670, L135
- Feigelson, E.D., & DeCampli, W.M. 1981, *ApJ*, 243, L89
- Fuente, A., Martín-Pintado, J., Rodríguez-Fernández, N.J., Rodríguez-Franco, A., De Vicente, P., & Kunze, D. 1999, *ApJ*, 518, L45
- Fuller, G.A., Ladd, E.F., Padman, R., Myers, P.C., & Adams, F.C. 1995, *ApJ*, 454, 862
- Gagné, M., Skinner, S.L., & Daniel, K.J. 2004, *ApJ*, 613, 393
- Gahm, G.F. 1980, *ApJ*, 242, L163
- García Lopez, R., Natta, A., Testi, L., & Habart, E. 2006, *A&A*, 459, 837
- Getman, K.V., Feigelson, E.D., Townsley, L., Bally, J., Lada, C.J., & Reipurth, B. 2002, *ApJ*, 575, 354
- Gibb, E.L., Van Brunt, K.A., Brittain, S.D., & Rettig, T.W. 2007, *ApJ*, 660, 1572
- Glassgold, A.E., Najita, J. & Igea, J. 2004, *ApJ*, 615, 972
- Gorti, U. & Hollenbach, D. 2004, *ApJ*, 613, 424
- Gorti, U. & Hollenbach, D. 2008, *astroph/0804.3381*
- Grasdalen, G.L., Sloan, G., Stout, N., Strom, S.E., & Welty, A.D. 1989, *ApJ*, 339, L37
- Güdel, M., et al. 2007, *A&A*, 468, 353
- Gullbring, E., Hartmann, L., Briceño, & Calvet, N. 1998, *ApJ*, 492, 323
- Gullbring, E., Hartmann, L., Briceño, C., & Calvet, N. 2000, *ApJ*, 492, 323
- Hartigan, P., Edwards, S., & Ghandour, L. 1995, *ApJ*, 452, 736
- Hartmann, L., & Kenyon, S.J. 1996, *ARA&A*, 34, 207
- Hartmann, L., Calvet, N., Gullbring, E., & D'Alessio, P. 1998, *ApJ*, 495, 385
- Herbertz, R., Ungerechts, H., & Winnewisser, G. 1991, *A&A*, 249, 483
- Herbig, G.H., & Dahm, S.E. 2006, *AJ*, 131, 1530
- Herbst, W., Racine, R., & Warner, J.W. 1978, *ApJ*, 223, 471
- Herczeg, G.J., Linsky, J.L., Valenti, J.A., Johns-Krull, C.M., & Wood, B.E. 2002, *ApJ*, 572, 310
- Herczeg, G.J., Wood, B.E., Linsky, J.L., Valenti, J.A., & Johns-Krull, C.M. 2004, *ApJ*, 607, 369
- Herczeg, G.J., Najita, J.R., Hillenbrand, L.A., & Pascucci, I. 2007, *ApJ*, 670, 509
- Hernández, J., Calvet, N., Briceño, C., Hartmann, L., & Berlind, P. 2004, *AJ*, 127, 1682
- Hinkle, K.H., Cuberly, R.W., Gaughan, N.A., Heynssens, J.B., Joyce, R.R., Ridgway, S.T., Schmitt, P., & Simmons, J.E. 1998, *Proc. SPIE*, 3354, 810
- Hogerheijde, M.R., van Dishoeck, E.F., Blake, G.A., & van Langevelde, H.J. 1998, *ApJ*, 502, 315
- Hollenbach, D., & McKee, C.F. 1979, *ApJS*, 41, 555
- Imanishi, K., Tsujimoto, M., & Katsuji, K. 2002, *ApJ*, 572, 300
- Isella, A., & Natta, A. 2005, *A&A*, 438, 899
- Jayawardhana, R., Fisher, R.S., Telesco, C.M., Piña, R.K., Barrado y Navascués, D., Hartmann, L.W., & Fazio, G.G. 2001, *AJ*, 122, 2047
- Jennings, D.E., Bragg, S.L., & Brault, J.W. 1984, *ApJ*, 282, L85
- Johns-Krull, C.M., Valenti, J.A., & Linsky, J.L. 2000, *ApJ*, 539, 815
- Jonkheid, B., Faas, F.G.A., van Zadelhoff, G.J., & van Dishoeck, E.F. *A&A*, 428, 511
- Kastner, J.H., Huenemoerder, D.P., Schultz, N.S., & Weintraub, D.A. 1999, *ApJ*, 525, 837
- Lacy, J.H., Knack, R., Geballe, T.R., & Tokunaga, A.T. 1994, *ApJ*, 428, L69
- Lacy, J.H., Richter, M.J., Greathouse, T.K., Jaffe, D.T., & Zhu, Q. 2002, *ApJ*, 114, 153
- Lahuis, F., van Dishoeck, E.F., Blake, G.A., Evans II, N.J., Kessler-Silacci, J.E., & Pontoppidan, K.M. 2007, *ApJ*, 665, 492
- Leinert, C., & Haas, M. 1989, *ApJ*, 342, L39
- Leinert, Ch., Beck, T.L., Ligor, S., Simon, M., Woitas, J., & Howell, R.R. 2001, *A&A*, 369, 215
- Liu, M.C., et al. 1996, *ApJ*, 461, 334
- Loinard, L., Torres, R.M., Mioduszewski, A.J., & Rodríguez, L.F. 2008, *ApJ*, 675, L29
- Lombardi, M., Lada, C.J., & Alves, J. 2008, *A&A*, 480, 785
- Lommen, D., Jørgensen, J.K., van Dishoeck, E.F., & Crapsi, A. 2008, *A&A*, 481, 141
- Loren, R.B., Wootten, A., & Wilking, B.A. 1990, *ApJ*, 365, 269
- Lucas, P.W., et al. 2004, *MNRAS*, 352, 1347
- Luhman, K.L., & Rieke, G.H. 1999, *ApJ*, 525, 440
- Mamajek, E.E. 2005, *ApJ*, 634, 1385
- Mamajek, E.E. 2008, *Astron. Nachr.*, 329, 10
- Mandy, M.E., & Martin, P.G. 1993, *ApJS*, 86, 199
- Mannings, V., & Sargent, A.I. 1997, *ApJ*, 490, 792
- Mariñas, N., Telesco, C.M., Fisher, R.S., Packham, C., & Radomski, J.T. 2006, *ApJ*, 653, 1353

- Martin-Zaïdi, C., Lagage, P.O., Pantin, E., & Habart, E. 2007, ApJ, 666, L117
- Marvel, K.B. 2005, AJ, 130, 2732
- Ménard, F., Monin, J.L., Angelucci, F. & Rouan, D. 1993, ApJ, 414, L117
- Mundt, R., Stocke, J., Strom, S.E., Strom, K.M., & Anderson, E.R. 1985, ApJ, 297, L41
- Mundy, L.G., et al. 1996, ApJ, 464, L169
- Najita, J., Carr, J.S., & Mathieu, R.D. 2003, ApJ, 589, 931
- Najita, J.R., Carr, J.S., Glassgold, A.E., Valenti, J.A. 2007a. In *Protostars and Planets V* ed. B. Reipurth, D. Jewitt, K. Keil. Tucson: Univ. Ariz. In press.
- Najita, J.R., Strom, S.E., & Muzerolle, J. 2007b, MNRAS, 378, 369
- Natta, A., Testi, L., & Randich, S. 2006, A&A, 452, 245
- Neuhauser, R., Sterzik, M.F., Schmitt, J.H.M.M., Wichmann, R., & Krautter, J. 1995, A&A, 297, 391
- Neufeld, D.A., & Hollenbach, D.J. 1994, ApJ, 428, 170
- Neufeld, D.A., Melnick, G.J., & Harwit, M. 1998, ApJ, 506, L75
- Nomura, H., & Millar, T.J. 2005, A&A, 438, 923
- Nomura, H., Aikawa, Y., Tsujimoto, M., Nakagawa, Y., & Millar, T.J. 2007, ApJ, 661, 334
- Pascucci, I., et al. 2006, ApJ, 651, 1177
- Pascucci, I., et al. 2007, ApJ, 663, 383
- Pontoppidan, K.M., Schiër, F.L., van Dishoeck, E.F., & Dartois, E. 2002, A&A, 393, 585
- Prato, L., Greene, T.P., & Simon, M. 2003, ApJ, 584, 853
- Pyo, T.-S., et al. 2006, ApJ, 649, 836
- Ramsay Howat, S.K., & Greaves, J.S. 2007, MNRAS, 379, 1658
- Ratzka, T., Leinert, C., Henning, T., Bouwman, J., Dullemond, C.P., & Jaffe, W. 2007, A&A, 471, 173
- Richter, M. J., Jaffe, D. T., Blake, G. A., & Lacy, J. H. 2002, ApJ, 572, L161
- Roberge, A., et al. 2001, ApJ, 551, L97
- Sako, S., Yamashita, T., Kataza, H., Miyata, T., Okamoto, Y.K., Honda, M., Fujiyoshi, T., & Onaka, T. 2005, ApJ, 620, 347
- Salyk, C., Pontoppidan, K.M., Blake, G.A., Lahuis, F., van Dishoeck, E.F., & Evans II, N.J. 2008, ApJ, 676, L49
- Semenov, D., Pavlyuchenkov, Y., Schreyer, K., Henning, T., Dullemond, C., & Bacmann, A. 2005, ApJ, 621, 853
- Sheret, I., Ramsey Howat, S.K., & Dent, W.R.F. 2003, MNRAS, 343, L65
- Siess, L., Forestini, M., & Gertout, C. 1999, A&A, 342, 480
- Shevchenko, V., Yakubov, S.D., Ambaryan, V.V., & Garibdzhanyan, A.T. 1991, Soviet Astr. 35, 135
- Skinner, S.L., Briggs, K.R., & Güdel, M. 2006, ApJ, 643, 995
- Stelzer, B., & Schmitt, J.H.H.M. 2004, A&A, 418, 687
- Stelzer, B., Micela, G., Hamaguchi, K., & Schmitt, J.H.M.M. 2006a, A&A, 457, 223
- Stelzer, B., Schmitt, J.H.M.M., Micela, G., & Liefke, C. 2006b, A&A, 460, L35
- Sternberg, A., & Neufeld, D.A. 1999, ApJ, 516, 371
- Strom, K.M., Strom, S.E., Edwards, S., Cabrit, S., & Skrutskie, M.F. 1989, AJ, 97, 1451
- Swartz, D.A., Drake, J.J., Elsner, R.F., Ghosh, K.K., Grady, C.A., Wassell, E., Woodgate, B.E., & Kimble, R.A. 2005, ApJ, 628, 811
- Takami, M., Beck, T.L., Pyo, T.-S., McGregor, P., & Davis, C. 2007, ApJ, 670, L33
- Tamura, M., Sato, S., Suzuki, H., Kaifu, N. & Hough, J.H. 1990, ApJ, 350, 728
- Thi, W.F., et al. 2001, ApJ, 561, 1074
- Thi, W.F. & Bik, A. 2005, A&A, 438, 557
- Tokunaga, A.T., et al. 2004, ApJ, 127, 444
- Uchida, K.I., et al. 2004, ApJS, 154, 439
- Valenti, J.A., Basri, G., & Johns, C.M. 1993, AJ, 106, 2024
- Valenti, J.A., Fallon, A.A., & Johns-Krull, C.M. 2003, ApJS, 147, 305
- van den Ancker, M.E., de Winter, D., & Tjin A Djie, H.R.E. 1998, A&A, 330, 145
- van den Ancker, M.E., Meeus, G., Cami, J., Waters, L.B.F.M., & Waelkens, C. 2001, A&A, 369, L17
- Wagenblast, R. 1992, MNRAS, 259, 155
- Wahhaj, Z., Koerner, D.W., & Sargent, A.I. 2007, ApJ, 661, 368
- Walter, F.M., & Kuhl, L.V. 1981, ApJ, 250, 254
- White, R.J., & Hillenbrand, L.A. 2004, ApJ, 616, 998
- Wilking, B.A., Lada, C.J., Young, E.T. 1989, ApJ, 340, 823
- Wilking, B.A., Bontemps, S., Schuler, R.E., Greene, T.P., & André, P. 2001, ApJ, 551, 357
- Ybarra, J.E., Barsony, M., Haisch Jr., K.E., Jarrett, T.H., Sahai, R., & Weinberger, A.J. 2006, ApJ, 647, L159
- Zuckerman, B. 2001, ARA&A, 39, 549

TABLE 1
PHYSICAL PROPERTIES OF THE STARS IN OUR SAMPLE

Star	RA	Dec	Sp.T.	Class	d (pc)	Age (Myr)	$\log L_x$ (erg s^{-1})	L_{FUV}^a (L_\odot)	\dot{M} ($10^{-7} M_\odot \text{ yr}^{-1}$)
49 Ceti	1 ^h 34 ^m 37 ^s .9	-15°40'35".5	A1	debris	61 ¹	7.8 ²	...	0.24 ³	...
51 Oph	17 ^h 31 ^m 25 ^s .0	-23°57'45".5	A0	HAeBe	131 ⁴	200 ⁵ ,0.3 ⁶	28.9 ⁷	13.6 ^{3,8}	1.35 ⁸
AB Aur	04 ^h 55 ^m 45 ^s .8	30°33'04".3	A0	HAeBe	144 ⁹	4.6 ²	29.5 ¹⁰	3.04 ³	1.41 ⁸
AS 209	16 ^h 49 ^m 15 ^s .3	-14°22'09".3	K5	II	119 ¹¹	...	30.4 ¹²	0.0058 ^{3,13}	...
AS 353a	17 ^h 56 ^m 21 ^s .2	-21°57'23".0	M1.5 ¹⁴	II	150 ¹⁵	0.2 ¹⁶	< 29.9 ¹⁷	...	39.8 ¹⁶
DoAr 21	16 ^h 26 ^m 03 ^s .0	-24°23'36".9	K0	III	119 ¹¹	0.3 ¹⁸	31.4 ¹⁹
Elias 29	16 ^h 27 ^m 09 ^s .5	-24°37'18".8	...	I	119 ¹¹	0.3 ¹⁸	< 28.7 ¹⁷	1.5	14.45 ²⁰
FU Ori	05 ^h 45 ^m 22 ^s .3	09°04'12".0	G3	fuori	500 ²¹	...	28.4 ²²	0.086 ^{3,23}	1900 ²¹
GG Tau	04 ^h 32 ^m 30 ^s .3	17°31'40".7	K6	II	140 ²⁴	1.7 ²	< 22.0 ²⁵	0.0075 ^{3,26}	0.175 ²⁶
GM Aur	04 ^h 55 ^m 10 ^s .9	30°21'59".5	K5	II	140 ²⁴	1.8 ²	29.6 ²⁷	0.0017 ^{3,26}	0.096 ²⁶
GSS 30	16 ^h 26 ^m 21 ^s .5	-24°23'07".8	...	I	119 ¹¹	0.3 ¹⁸	< 28.3 ²⁸
GV Tau N	04 ^h 29 ^m 23 ^s .7	24°32'57".6	K3	I	140 ²⁴	...	29.8 ¹⁰	0.21	1.95 ²⁹
GW Ori	05 ^h 29 ^m 08 ^s .4	11°52'12".7	K3	II	450 ³⁰	1.0 ³¹	31.7 ²⁷	0.31 ^{3,31}	2.85 ³¹
HD 141569	15 ^h 49 ^m 57 ^s .7	-03°55'17".0	B9.5	HAeBe	99 ⁴	> 10.0 ⁹	< 28.1 ³²	0.486 ³	0.043 ⁸
HD 163296	17 ^h 56 ^m 21 ^s .3	-21°57'23".0	A1	HAeBe	122 ⁴	6.0 ²	29.6 ³²	0.267 ³	0.001 ³³
HL Tau	04 ^h 31 ^m 38 ^s .5	18°13'58".0	K9	I	140 ²⁴	0.77 ³⁴	30.6 ¹⁰	0.17	1.6 ²⁹
IRAS 04278+2253	04 ^h 30 ^m 50 ^s .7	23°00'11".1	F1	I	140 ²⁴	7.1	66.1 ²⁹
L1551 IRS 5	04 ^h 31 ^m 34 ^s .2	18°08'05".3	G-K ³⁵	I	140 ²⁴	...	28.3 ¹⁰	...	< 140 ³⁶
LkCa 15	04 ^h 39 ^m 17 ^s .8	22°21'03".5	K5	III	140 ²⁴	11.7 ²	< 22.6 ²⁵	0.0056 ^{37,38}	0.068 ³⁹
Lk H α 225	20 ^h 20 ^m 30 ^s .8	41°21'24".8	...	HAeBe	1000 ⁴⁰
MWC 758	05 ^h 30 ^m 27 ^s .4	25°19'56".8	A3	HAeBe	200 ⁹	0.073 ³	...
RW Aur	05 ^h 07 ^m 49 ^s .6	30°24'05".4	G5	I	140 ²⁴	2.57 ³⁴	< 29.4 ⁴¹	0.065 ^{3,13}	15.8 ¹⁶
SVS 13	03 ^h 29 ^m 03 ^s .6	31°16'01".2	...	I	300 ⁴²	...	< 30.3 ⁴³	0.67	6.3 ⁴⁴
TW Hya	11 ^h 01 ^m 51 ^s .9	-34°42'18".3	K7	II	51 ⁴⁵	10 ⁴⁶	29.7 ⁴⁷	0.0017	0.018 ^{48,49}
V892 Tau	04 ^h 18 ^m 40 ^s .7	28°19'16".2	A6	HAeBe	140 ²⁴	...	30.9 ¹⁰	0.36	...
V1057 Cyg	20 ^h 58 ^m 53 ^s .1	44°15'28".6	...	fuori	600 ²¹	...	< 31.0 ¹⁷	0.21 ^{3,23}	...
V1331 Cyg	21 ^h 01 ^m 09 ^s .1	50°21'45".2	G5	fuori	550 ⁵⁰	0.8 ²³	< 30.9 ¹²
VV Ser	18 ^h 28 ^m 47 ^s .8	00°08'39".7	A2	HAeBe	245 ⁵¹	5.12 ^{3,8}	4.57 ⁸
Z CMa	07 ^h 03 ^m 42 ^s .0	-11°33'02".8	F6 ⁹	fuori	1150 ⁵²	...	30.3 ³²	5.96 ^{3,53}	790 ²¹

REFERENCES. — ¹Jayawardhana et al. (2001), ²Thi et al. (2001), ³Valenti et al. (2003), ⁴Hipparcos, ⁵van den Ancker et al. (2001), ⁶Herbertz et al. (1991), ⁷Berghöfer et al. (1996), ⁸Garcia Lopez et al. (2006), ⁹van den Ancker et al. (1998), ¹⁰Güdel et al. (2007), ¹¹Lombardi et al. (2008), ¹²Walter & Kuhi (1981), ¹³Valenti et al. (1993), ¹⁴Tokunaga et al. (2004), ¹⁵Prato et al. (2003), ¹⁶Hartigan et al. (1995), ¹⁷Carkner et al. (1998), ¹⁸Luhman & Rieke (1999), ¹⁹Imanishi et al. (2002), ²⁰Natta et al. (2006), ²¹Hartmann & Kenyon (1996), ²²Skinner et al. (2006), ²³Herbig & Dahm (2006), ²⁴Elias (1978), ²⁵Neuhauser et al. (1995), ²⁶Gullbring et al. (1998), ²⁷Feigelson & DeCampli (1981), ²⁸Gagné et al. (2004), ²⁹White & Hillenbrand (2004), ³⁰Dolan & Mathieu (2001), ³¹Calvet et al. (2004), ³²Stelzer et al. (2006b), ³³Swartz et al. (2005), ³⁴Siess et al. (1999), ³⁵Mundt et al. (1985), ³⁶Fuller et al. (1995), ³⁷Bergin et al. (2004), ³⁸Españolat et al. (2007), ³⁹Hartmann et al. (1998), ⁴⁰Marvel (2005), ⁴¹Gahm (1980), ⁴²Cernis (1990), ⁴³Getman et al. (2002), ⁴⁴Edwards et al. (2003), ⁴⁵Mamajek (2005), ⁴⁶Uchida et al. (2004), ⁴⁷Stelzer & Schmitt (2004), ⁴⁸Alencar & Batalha (2002), ⁴⁹Herczeg et al. (2004), ⁵⁰Shevchenko et al. (1991), ⁵¹Chavarría et al. (1988), ⁵²Herbst et al. (1978), ⁵³Stelzer et al. (2006a)

^a If not otherwise noted, value derived using TW Hya IUE Spectrum then scaling by relative accretion rates.

TABLE 2
 SUMMARY OF LINE DETECTIONS

Star	Instrument	λ (μm)	Date	Cont. (Jy)	Line Flux ^a	Line Luminosity ($10^{-6} L_{\odot}$)	Equivalent Width (km s^{-1})	FWHM (km s^{-1})
AB Aur	TEXES/IRTF	12.279	dec02,dec03	12.7 ^b	0.93 (0.25)	6.0	0.86 (0.23)	7.0
AB Aur	TEXES/Gemini	8.025	nov06	12.7 ^b	1.47 (0.34)	9.5	0.93 (0.21)	10.4
		12.279	nov06	14.7 ^b	0.53 (0.07)	3.4	0.44 (0.06)	8.5
		17.035	nov06	24.6 ^b	1.10 (0.3)	7.1	0.76 (0.21)	9.0
AB Aur	TEXES/Gemini	8.025	oct07	12.7 ^b	< 1.24 ^e	< 8.0
		12.279	oct07	14.7 ^b	0.56 (0.07)	3.6	0.47 (0.06)	9.4
		17.035	oct07	24.6 ^b	0.57 (0.16)	3.7	0.29 (0.08)	6.5
AB Aur	NIRSPEC/Keck	4.695	jan01-dec02	9.6 ^b	0.90 (0.07)	5.8	1.02 (0.08)	15.9
DoAr 21	TEXES/IRTF	12.279	jun03	0.14 ^b	0.33 (0.09)	1.5	24.06 (6.46)	5.6
Elias 29	TEXES/IRTF	12.279	jun03	24.0 ^c	2.45 (0.33)	10.9	1.27 (0.17)	15.1
		17.035	jun03	30.5 ^c	1.64 (0.30)	7.3	0.94 (0.18)	11.9
Elias 29	TEXES/Gemini	12.279	jul06	24.0 ^c	0.70 (0.12)	3.1	0.36 (0.06)	12.7
Elias 29	NIRSPEC/Keck	4.695	jul00-apr05	22.9 ^b	2.12 (0.33)	9.4	0.44 (0.07)	21.8
GSS 30	TEXES/IRTF	12.279	jun03	14.7 ^d	1.19 (0.25)	5.3	0.98 (0.21)	6.8
GSS 30	TEXES/Gemini	8.025	jul06	4.21 ^d	0.78 (0.07)	3.5	1.50 (0.14)	14.7
		12.279	jul06	14.7 ^d	1.13 (0.14)	5.0	0.95 (0.12)	10.5
GSS 30	NIRSPEC/Keck	4.695	apr02	1.2 ^b	1.97 (0.17)	8.7	7.38 (0.62)	28.0
GV Tau N	TEXES/Gemini	12.279	nov06	25.6 ^b	0.55 (0.07)	3.4	0.27 (0.04)	8.5
HL Tau	TEXES/IRTF	12.279	dec02	7.6 ^c	1.16 (0.18)	7.1	1.82 (0.29)	10.9
HL Tau	TEXES/Gemini	8.025	nov06	5.5 ^c	0.34 (0.11)	2.1	0.50 (0.16)	7.1
		12.279	nov06	7.6 ^c	0.84 (0.13)	5.1	1.36 (0.22)	12.3
		17.035	nov06	13.4 ^c	0.84 (0.23)	5.1	1.07 (0.29)	11.6
HL Tau	NIRSPEC/Keck	4.695	oct01-nov03	1.6 ^b	0.09 (0.03)	0.6	0.27 (0.06)	11.9

^a In units of 10^{-14} ergs s^{-1} cm^{-2} , Value in parentheses is $1-\sigma$ error

^b Measured value

^c ISO SWS archive

^d *Spitzer* IRS

^e 3σ limit assuming FWHM = 10.4 km s^{-1}

TABLE 3
RESULTS OF LTE MODEL FITS

Star	Telescope	One Component		Two Component			
		Temperature (K)	Mass (M_{\oplus})	T_{cold} (K)	M_{cold} (M_{\oplus})	T_{hot} (K)	M_{hot} (M_{\oplus})
AB Aur ^a	Gemini	670 (40)	0.52 (0.15)	320 (60)	1.65 (0.52)	1470 (100)	0.076 (0.01)
GSS 30 ^a	Gemini	535 (45)	0.78 (0.16)	520 (60)	0.82 (0.27)	3330 (130)	0.002 ^{+0.002} _{-0.0007}
HL Tau ^a	Gemini	465 (20)	1.09 (0.14)	460 (20)	1.11 (0.17)	1790 ⁺⁶⁰ ₋₄₄₀	0.001 ^{+0.004} _{-0.001}
Elias 29 ^b	Gemini	1210 (90)	0.19 (0.03)
Elias 29 ^b	IRTF	1000 (90)	0.78 (0.07)

^a One component fit to S(1), S(2), and S(4). Two component fit includes S(9).

^b One component fit to S(1), S(2), and S(9).

TABLE 4
 SUMMARY OF UPPER LIMITS - IRTF/TEXES

Star	λ (μm)	Date	F_{ν} ^a (Jy)	Line Flux ^b	Mass in M_{Jup}		
					200 K	500 K	800 K
51 Oph	12.279	jun03	10.9	< 2.2	< 1.84	< 3.0×10^{-2}	< 1.3×10^{-2}
AB Aur	8.025	oct04	12.9	< 1.2	< 449.1	< 3.3×10^{-2}	< 3.9×10^{-3}
	17.035	dec02, jan04	25.2	< 1.1	< 4.5×10^{-2}	< 5.4×10^{-3}	< 4.0×10^{-3}
AS 209	12.279	jun03	2.5	< 0.61	< 4.2×10^{-1}	< 6.8×10^{-3}	< 3.1×10^{-3}
AS 353	17.035	jun03, jul03	1.6	< 1.6	< 7.1×10^{-2}	< 8.5×10^{-3}	< 6.4×10^{-3}
FU Ori	12.279	jan04, jan05	6.4	< 0.8	< 9.7	< 1.6×10^{-1}	< 7.1×10^{-2}
	17.035	jan05	5.8	< 3.0	< 1.5	< 1.8×10^{-1}	< 1.3×10^{-1}
GG Tau	12.279	jan04	1.6	< 2.1	< 2.0	< 3.2×10^{-2}	< 1.5×10^{-2}
	17.035	nov01	0.5	< 2.8	< 1.1×10^{-1}	< 1.3×10^{-2}	< 9.7×10^{-3}
GW Ori	12.279	dec00, jan05	8.6	< 1.1	< 10.8	< 1.7×10^{-1}	< 7.9×10^{-2}
	17.035	nov01	4.9	< 2.8	< 1.1	< 1.3×10^{-1}	< 1.0×10^{-1}
HD 163296	12.279	jun03, jul03	11.4	< 0.6	< 4.3×10^{-1}	< 7.0×10^{-3}	< 3.2×10^{-3}
	17.035	jul03	13.7	< 2.35	< 6.9×10^{-2}	< 8.3×10^{-3}	< 6.2×10^{-3}
IRAS 04278+2253	12.279	jan04, jan05	8.0	< 0.62	< 5.9×10^{-1}	< 9.5×10^{-3}	< 4.3×10^{-3}
	17.035	jan05	10.7	< 2.8	< 1.1×10^{-1}	< 1.3×10^{-2}	< 9.7×10^{-3}
L1551 IRS 5	12.279	dec02	13.2	< 1.4	< 1.3	< 2.1×10^{-2}	< 9.7×10^{-3}
	17.035	nov00	20.0	< 1.9	< 7.4×10^{-2}	< 8.8×10^{-3}	< 6.6×10^{-3}
Lk H α 225	12.279	jun03	37.9	< 2.5	< 121.7	< 2.0	< 8.9×10^{-1}
	17.035	oct04	48.2	< 3.56	< 7.1	< 8.4×10^{-1}	< 6.3×10^{-1}
SVS 13	12.279	dec02	13.3	< 1.02	< 4.5	< 7.2×10^{-2}	< 3.3×10^{-2}
	17.035	dec02	18.8	< 2.0	< 3.6×10^{-1}	< 4.3×10^{-2}	< 3.2×10^{-2}
V892 Tau	12.279	jan04	31.2	< 3.0	< 2.86	< 4.6×10^{-2}	< 2.1×10^{-2}
	17.035	dec02	71.7	< 4.9	< 1.9×10^{-1}	< 2.2×10^{-2}	< 1.7×10^{-2}
V1057 Cyg	12.279	oct04	7.0	< 0.8	< 14.0	< 2.3×10^{-1}	< 1.0×10^{-1}
Z CMa	12.279	dec03	142.6	< 3.7	< 238.3	< 3.8	< 1.74
	17.035	dec02	170.8	< 14.0	< 36.8	< 4.4	< 3.27

^a Measured TEXES flux value

^b 3σ limit in units of 10^{-14} ergs s⁻¹ cm⁻²

TABLE 5
SUMMARY OF UPPER LIMITS - GEMINI/TEXES

Star	λ (μm)	Date	F_ν (Jy)	Line Flux ^{a,b}	Mass in M_{Jup}		
					200 K	500 K	800 K
49 Ceti	12.279	nov06	0.2 ^c	< 0.17	< 3.1×10^{-2}	< 5.0×10^{-4}	< 2.2×10^{-4}
	17.035	nov06	0.19 ^c	< 0.88	< 6.5×10^{-3}	< 7.7×10^{-4}	< 5.8×10^{-4}
AS 209	12.279	jul06	2.0 ^d	< 0.34	< 2.3×10^{-1}	< 3.8×10^{-3}	< 1.7×10^{-3}
	17.035	jul06	4.4 ^e	< 1.03	< 2.9×10^{-2}	< 3.4×10^{-3}	< 2.6×10^{-3}
AS 353	12.279	jul06	1.11 ^f	< 0.29	< 3.2×10^{-1}	< 5.1×10^{-3}	< 2.3×10^{-3}
DoAr 21	12.279	jul06	0.14 ^g	< 0.18	< 8.4×10^{-1}	< 1.4×10^{-2}	< 6.1×10^{-3}
Elias 29	17.035	jul06	30.5 ^e	< 1.36	< 3.8×10^{-2}	< 4.6×10^{-3}	< 3.4×10^{-3}
FU Ori	8.025	nov06	3.5 ^g	< 1.14	< 5143.6	< 3.8×10^{-1}	< 4.5×10^{-2}
	12.279	nov06	3.6 ^g	< 0.22	< 2.7	< 4.3×10^{-2}	< 2.0×10^{-2}
GM Aur	12.279	nov06	0.25 ^h	< 0.54	< 5.2×10^{-1}	< 8.3×10^{-3}	< 3.8×10^{-3}
GSS 30	17.035	jul06	30.75 ^f	< 1.3	< 3.7×10^{-2}	< 4.3×10^{-3}	< 3.3×10^{-3}
HD 141569	12.279	jul06	1.13 ^e	< 2.75	< 1.3	< 2.1×10^{-2}	< 9.6×10^{-3}
HD 163296	12.279	jul06	14.2 ^e	< 1.18	< 8.6×10^{-1}	< 1.4×10^{-2}	< 6.2×10^{-3}
	17.035	jul06	21.6 ^e	< 2.42	< 7.2×10^{-2}	< 8.5×10^{-3}	< 6.4×10^{-3}
LkCa 15	12.279	nov06	0.12 ^g	< 0.08	< 7.6×10^{-2}	< 1.2×10^{-3}	< 5.6×10^{-4}
	17.035	nov06	0.48 ^e	< 0.97	< 3.8×10^{-2}	< 4.5×10^{-3}	< 3.3×10^{-3}
MWC 758	17.035	nov06	3.8 ^e	< 0.65	< 5.2×10^{-2}	< 6.1×10^{-3}	< 4.6×10^{-3}
RW Aur	8.025	nov06	0.07 ^f	< 0.37	< 130.9	< 9.7×10^{-3}	< 1.1×10^{-3}
	17.035	nov06	1.87 ^f	< 0.29	< 1.1×10^{-2}	< 3.7×10^{-2}	< 1.0×10^{-3}
TW Hya	12.279	feb06	0.5 ⁱ	< 0.6	< 7.6×10^{-2}	< 1.2×10^{-3}	< 5.5×10^{-4}
	17.035	feb06	1.4 ⁱ	< 0.7	< 8.9×10^{-2}	< 1.4×10^{-3}	< 6.5×10^{-4}
V 1331 Cyg	17.035	nov06	1.65 ^f	< 0.52	< 3.1×10^{-1}	< 3.7×10^{-2}	< 2.8×10^{-3}
VV Ser	12.279	jul06	4.61 ^h	< 0.55	< 1.6	< 2.6×10^{-2}	< 1.2×10^{-2}
	17.035	jul06	2.6 ^g	< 1.2	< 1.4×10^{-1}	< 1.7×10^{-2}	< 1.3×10^{-2}

^a 3σ limit in units of 10^{-14} ergs s^{-1} cm^{-2}

^b Upper limits calculated assuming FWHM=5.5 km s^{-1} for TW Hya, 10 km s^{-1} for others

^c Wahhaj et al. (2007)

^d Liu et al. (1996)

^e ISO SWS archive

^f Spitzer IRS

^g Measured TEXES flux value

^h IRAS

ⁱ Ratzka et al. (2007)

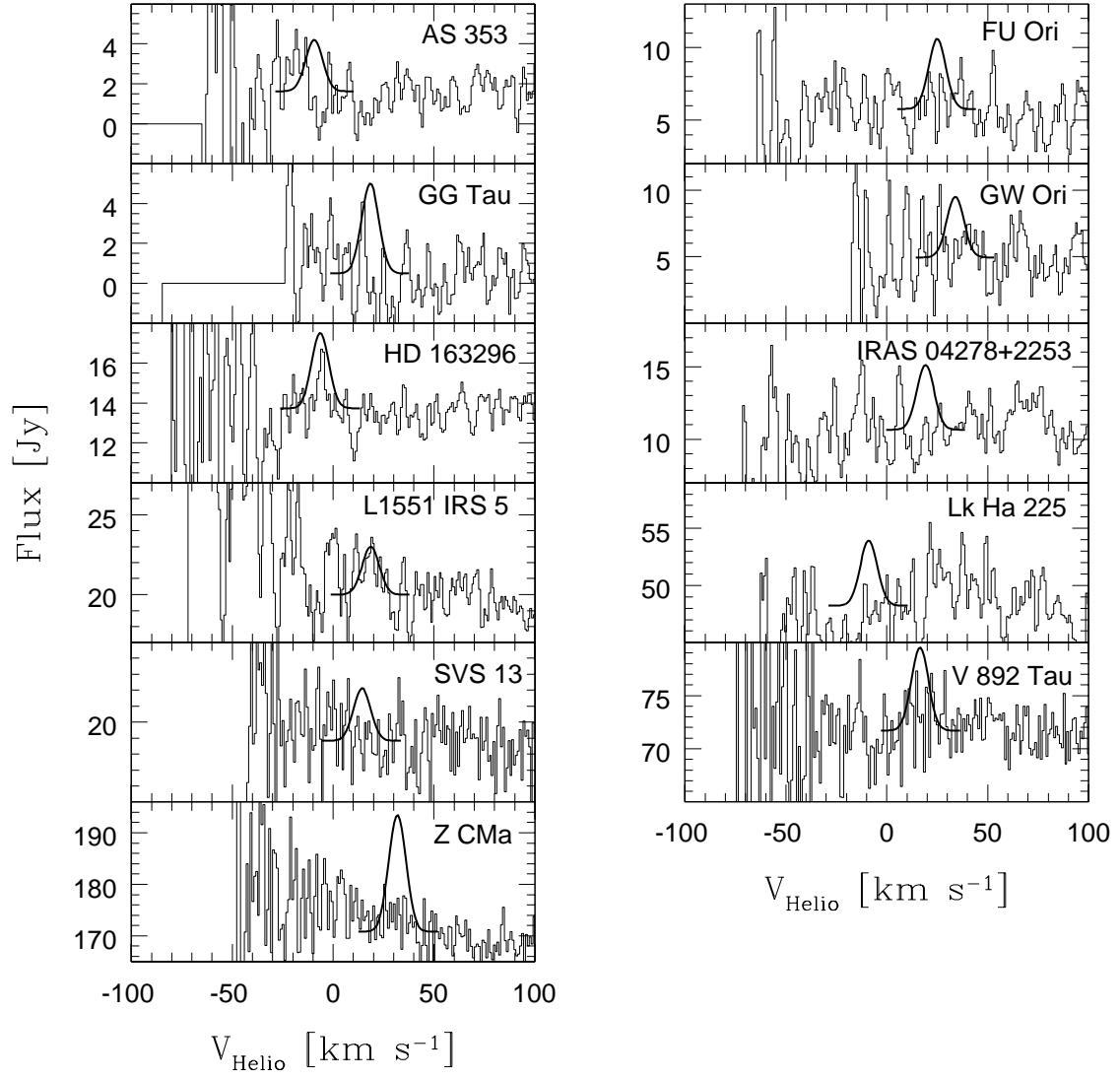


FIG. 13.— Upper limits for IRTF H₂ S(1) observations near 17 μm . The overplotted Gaussian is centered at the stellar velocity of each source and represents the $3\text{-}\sigma$ upper limit based on an assumed FWHM of 10 km s^{-1} .

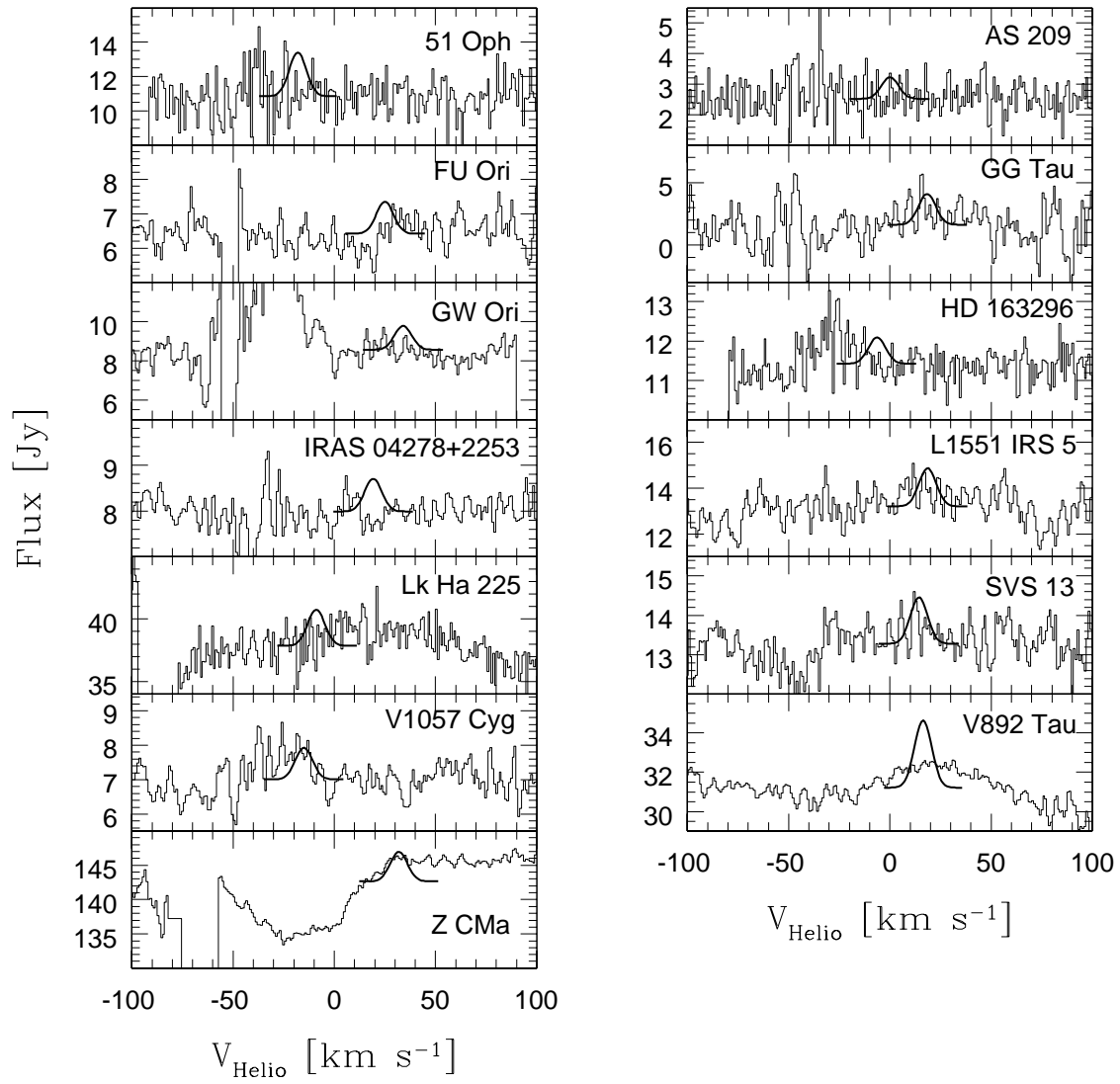


FIG. 14.— Upper limits for IRTF H₂ S(2) observations near 12 μm . The overplotted Gaussian is centered at the stellar velocity of each source and represents the 3- σ upper limit based on an assumed FWHM of 10 km s⁻¹.

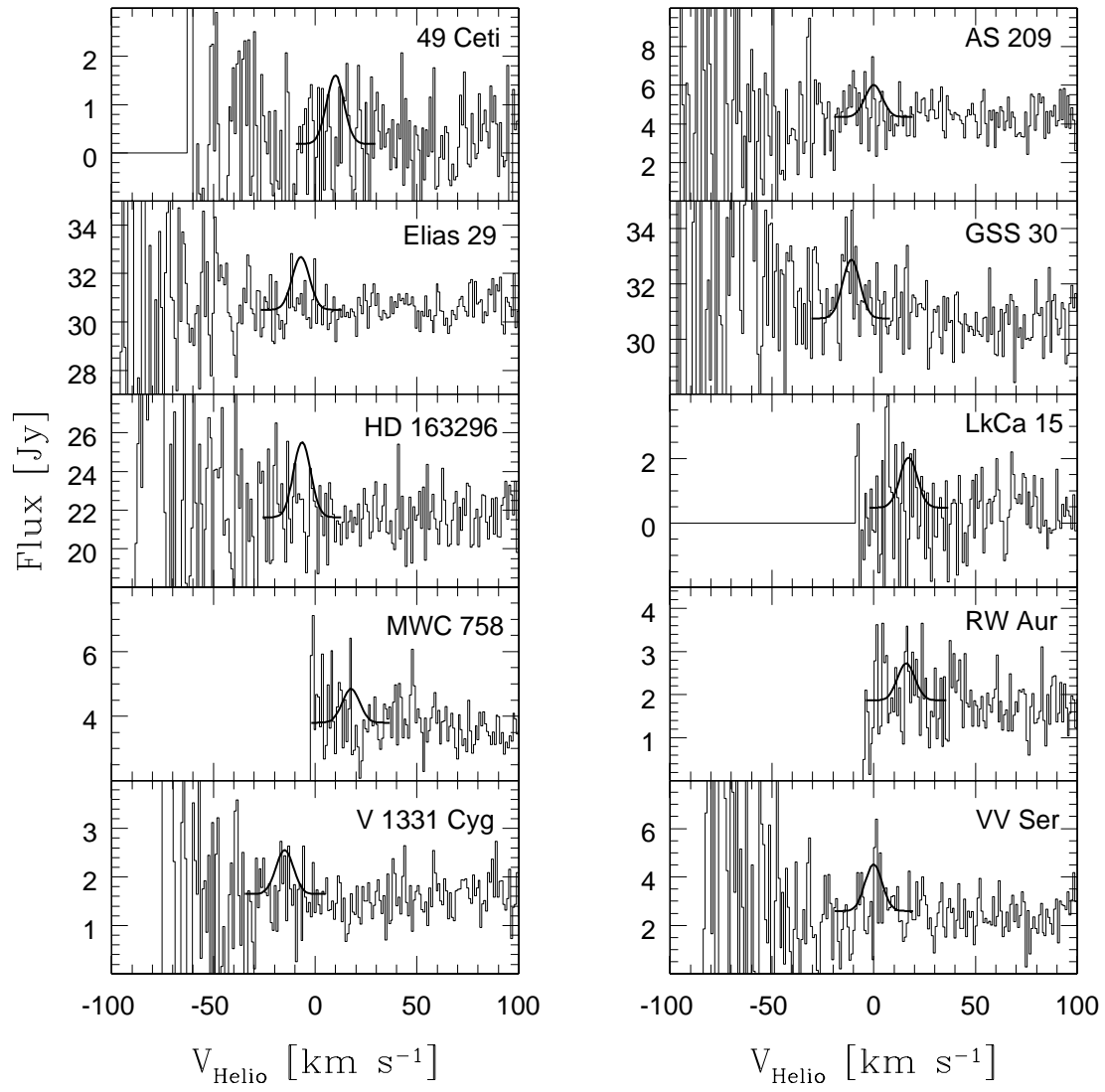


FIG. 15.— Upper limits for Gemini H₂ S(1) observations near $17 \mu\text{m}$. The overplotted Gaussian is centered at the stellar velocity of each source and represents the $3\text{-}\sigma$ upper limit based on an assumed FWHM of 10 km s^{-1} .

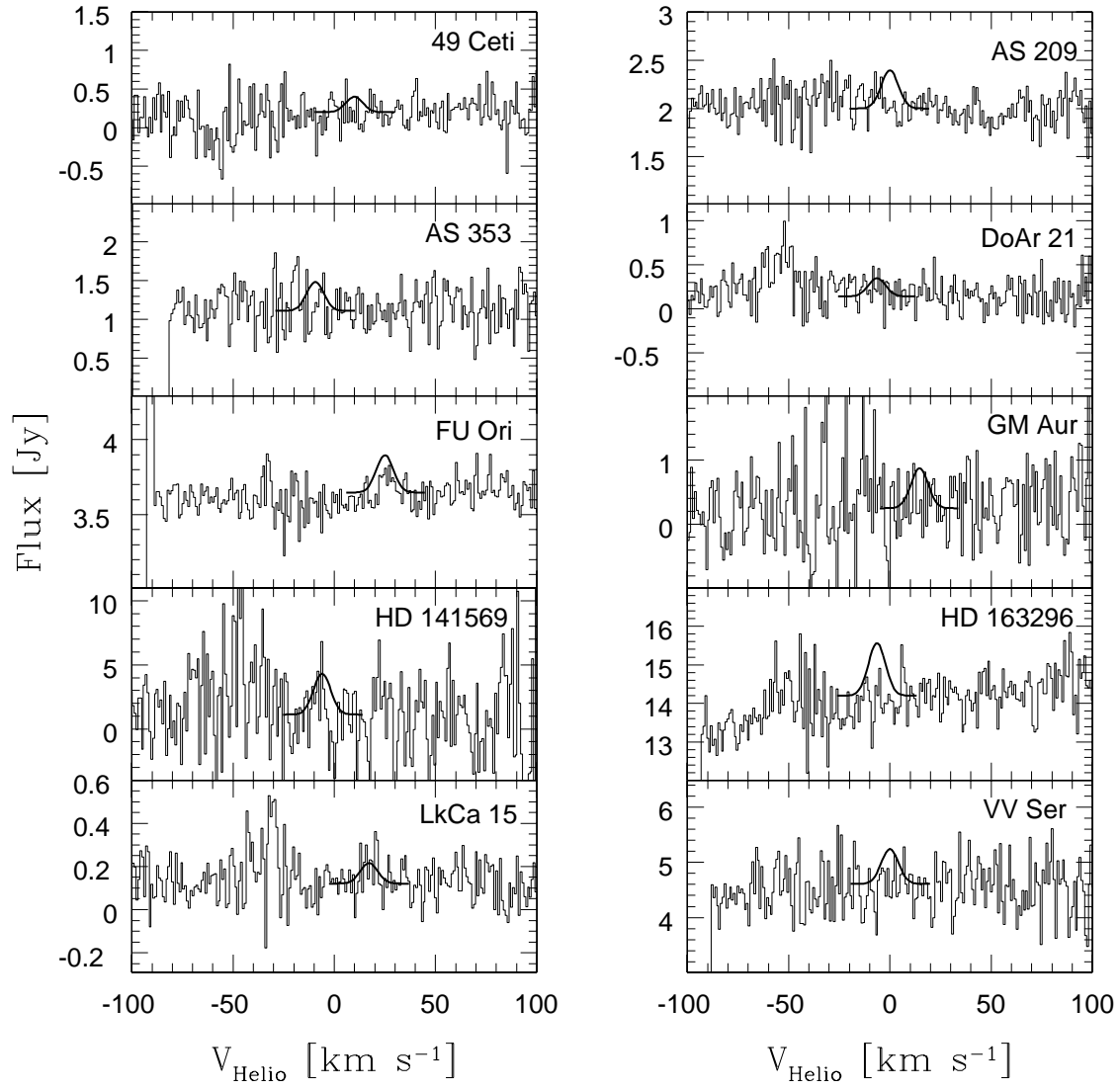


FIG. 16.— Upper limits for Gemini H₂ S(2) observations near 12 μm . The overplotted Gaussian is centered at the stellar velocity of each source and represents the 3- σ upper limit based on an assumed FWHM of 10 km s⁻¹.

APPENDIX
 ACCRETION SHOCK HEATING

The total luminosity L from a shock of area A is given by:

$$L = \frac{1}{2} \rho_o v_s^3 A, \quad (\text{A1})$$

where ρ_o is the preshock mass density and v_s is the shock velocity (the normal component of the velocity of the flow with respect to the shock surface). The mass accretion rate \dot{M}_{acc} through the shock is given by:

$$\dot{M}_{acc} = \rho_o v_s A = m_p n_o v_s A, \quad (\text{A2})$$

where n_o is the gas hydrogen nucleus number density and m_p is the mass per hydrogen nucleus ($\sim 2.3 \times 10^{-24}$ gm). Therefore, the luminosity can be rewritten

$$L = \frac{1}{2} \dot{M}_{acc} v_s^2. \quad (\text{A3})$$

However, in an accretion shock onto an optically thick disk, where one half of the radiation is emitted toward the disk midplane and is absorbed, the escaping luminosity is given by (see Neufeld & Hollenbach 1994):

$$L_{disk} = \frac{1}{4} \dot{M}_{acc} v_s^2. \quad (\text{A4})$$

The shock velocity is on the order of (but somewhat smaller due to the oblique incident angle of the infall to the shock front) the freefall velocity onto the disk, or, for our $r > 10$ AU constraint, $v_s \sim 5 - 10$ km s⁻¹. Assuming the accretion rate from the core onto the disk through the accretion shock is similar to the accretion rate from the disk onto the star, the measured accretion rates for our sources are of order $\dot{M}_{acc} \sim 10^{-7}$ M_⊙ yr⁻¹. Therefore,

$$L_{disk} \simeq 4 \times 10^{-4} \dot{M}_{-7} v_{s6}^2 L_{\odot}, \quad (\text{A5})$$

where $\dot{M}_{-7} \equiv \dot{M}_{acc}/10^{-7}$ M_⊙ yr⁻¹ and $v_{s6} \equiv v_s/10^6$ cm s⁻¹ = $v_s/10$ km s⁻¹.

To determine the luminosity in the pure rotational lines of H₂, one needs the fraction f_J of the total shock luminosity that emerges in the H₂ 0-0 S(J) line. This fraction depends on the preshock density n_o , the shock velocity v_s , the amount of depletion of the preshock gas coolants, and whether the shock is ‘‘C type’’ (Draine 1980) or ‘‘J type’’ (cf. Hollenbach & McKee 1979). The preshock density can be estimated by taking the shock area A to be at least $2\pi r_s^2 \sim 1.4 \times 10^{29}$ cm², with $r_s \sim 10$ AU and the factor of 2 to account for both sides of the disk. Using Eq. (2), we obtain

$$n_o \simeq 3 \times 10^6 \dot{M}_{-7} v_{s6}^{-1} A_{30}^{-1} \text{ cm}^{-3}, \quad (\text{A6})$$

with $A_{30} = A/10^{30}$ cm². Burton et al. (1992) present results for J shocks with $n_o = 10^6$ cm⁻³ and $v_s = 5 - 10$ km s⁻¹ in terms of the intensity I_J of an H₂ 0-0 S(J) line. Here,

$$f_J = \frac{4\pi I_J}{0.5 m_p n_o v_s^3}. \quad (\text{A7})$$

They show cases with high abundances of gas phase oxygen not in CO and with extremely low abundances of gas phase oxygen not in CO. The latter case is perhaps more realistic since oxygen not in CO is expected to freeze out as water ice in dense cores, and a slow 5-10 km s⁻¹ shock does not release water from the ice mantles to the gas (Hollenbach & McKee 1979). In the former case, the gas phase oxygen not in CO rapidly converts to gas phase H₂O in the shock, and the H₂O dominates the shock cooling and thereby weakens the H₂ lines. Burton et al. (1992, see Figures 5b and 6) find that for the case with H₂O freezeout $f_1 \sim 2.5 \times 10^{-3}$, $f_2 \sim 2.5 \times 10^{-3}$ and $f_3 \sim 10^{-2}$. In the case with abundant gas phase oxygen not in CO, $f_1 \sim 10^{-4}$, $f_2 \sim 10^{-4}$, and $f_3 \sim 10^{-3}$. Burton et al. (1992) do not present results for f_4 , but inspection of the unpublished output of these runs reveals $f_4 \sim 0.5 f_3$. A lower v_s results in lower ratios of f_4/f_2 .

Draine et al. (1983) present I_J for C type shocks with $n_o = 10^6$ cm⁻³, preshock magnetic field component parallel to the shock front $B_o = 0.5$ mG, electron abundance $x_e = 10^{-8}$, and where gas phase oxygen not in CO is *not* depleted. Their result at $v_s = 10$ km s⁻¹ implies $f_1 \sim 10^{-2}$, $f_2 \sim 4 \times 10^{-3}$, and $f_3 \sim 10^{-2}$. They also do not present results for f_4 , but we again estimate $f_4 \sim 0.5 f_3$. Presumably, these fractions would be somewhat larger if oxygen is allowed to freezeout as water ice.

From the above results, we see for J shocks with water ice freezeout and for C shocks, the luminosities in the H–2 0-0 S(1), S(2) and S(4) lines are $\sim 10^{-6} - 10^{-5} \dot{M}_{-7} v_{s6}^2 L_{\odot}$. These luminosities (assuming $\dot{M}_{-7} \sim 1$ correspond to our observed luminosities, suggesting accretion shocks as a viable excitation mechanism for these emission lines. For J shocks without freezeout the luminosities are about an order of magnitude less than observed for $\dot{M}_{-7} \sim 1$.

These same shock results can be used to estimate the intensities of CO mid J transitions in the shocks. Burton et al. (1992) show that in the J shocks presented here the CO J= 17-16 transition is ~ 3 times stronger than the H₂ 0-0 S(1) line. Draine & Roberge (1984) and Draine et al. (1983) present C shock models from which the CO J \rightarrow J-1 line strengths can be estimated. For $n_o = 10^6 \text{ cm}^{-3}$, $v_s = 10 \text{ km s}^{-1}$, and B_o and x_e from above, the CO J \rightarrow J-1 line intensities peak at J $\sim 10 - 12$ with strengths comparable to that of H₂ 0-0 S(1). Thus, Herschel observations of these disks with the HIFI instrument may detect the submillimeter CO lines near the J peak, validate the shock models, and constrain the shock parameters such as n_o , v_s , and A .

It is difficult to estimate the strengths of lines other than those of H₂ and CO because their strength depends on their gas phase abundances, and all species other than the undepleted H₂ and CO (e.g., Fe, Fe⁺, S, O) may be heavily depleted on grains as ice mantles and/or refractory material. Such slow shocks are unlikely to remove them. Radiative transfer calculations need to be performed to see if the dust grains are warm enough to thermally sublimate the ice mantles at distances of 10-30 AU from the star. A more detailed shock modeling of some of these observed sources is warranted.